MEASUREMENT REALITIES OF CURRENT COLLECTION IN DYNAMIC SPACE PLASMA ENVIRONMENTS

E. P. Szuszczewicz

Laboratory for Atmospheric and Space Sciences
Science Applications International Corporation
McLean, Virginia

Abstract

Theories which describe currents collected by conducting and non-conducting bodies immersed in plasmas have many of their concepts based upon the fundamentals of sheath-potential distributions and charged-particle behavior in superimposed electric and magnetic fields. Those current-collecting bodies (or electrodes) may be Langmuir probes, electric field detectors, aperture plates on ion mass spectrometers and retarding potential analyzers, or spacecraft and their rigid and tethered appendages. Often the models are incomplete in representing the conditions under which the current-voltage characteristics of the electrode and its system are to be measured. In such cases, the experimenter must carefully take into account magnetic field effects and particle anisotropies, perturbations caused by the current collection process itself and contamination on electrode surfaces, the complexities of non-Maxwellian plasma distributions, and the temporal variability of the local plasma density, temperature, composition and fields. This set of variables is by no means all-inclusive, but it represents a collection of circumstances guaranteed to accompany experiments involving energetic particle beams, plasma discharges, chemical releases, wave injection and various events of controlled and uncontrolled spacecraft charging. This paper attempts to synopsize these diagnostic challenges and frame them within a perspective that focuses on the physics under investigation and the requirements on the parameters to be measured. Examples will include laboratory and spaceborne applications, with specific interest in dynamic and unstable plasma environments.

1. Introduction

Electrical currents and associated current-collection characteristics are fundamental manifestations of charged-particle density and energy distibution functions, their collisionality in a host medium and their interactions with electric and magnetic fields. In naturally-occurring space plasmas we have current systems everywhere, from the Sun's photospheric and chromospheric domains, to the Earth's geoplasma region where the magnetosphere and the ionosphere are interactively coupled through the Birkland current system. In man-made systems focused on the interests of plasma physics in general, and space plasmas in particular, we have currents in electrode-type discharges (e.g., hollow-cathode discharges), currents to Langmuir probes, and other charged-particle detectors, and currents to a spacecraft body and tethered satellite configurations.

The current collected by any body immersed in a plasma (e.g., a satellite, an antenna, or a Langmuir probe) is controlled by the size and geometry of the body,

surface materials and levels of surface contamination, body aspect and velocity relative to the plasma and ambient fields, and of course the potential of the body itself.[1-5] On the other hand, the details of the plasma response function are controlled by the electric and magnetic fields and the electron and ion densities, the ion composition, the energy distribution functions and collision frequencies. Our best understood plasma-electrode systems are the simplest ones. Such systems generally involve:

a) "Perfect" body geometries (i.e., cylinders, spheres and "infinite" planes), with contamination-free perfectly-conducting surfaces that have a unity accommodation coefficient for every impinging charged particle;

b) Zero velocity of the body relative to the plasma, no magnetic fields, and potentials $< 25kT_e/e$ or < 50 volts, whichever is less; and

c) A neutral, quiescent, collisionless, non-drifting, fully-Maxwellian plasma with a single ion constituent.

However, most scientific interests focus on practical systems that at times bear little resemblance to the ideal simple system. A preponderance of investigations involve "imperfect" moving bodies (e.g., a satellite with a multitude of appendages and an admixture of conducting and non-conducting surface materials), high potentials (except for probes and particle detectors), and local sources of surface contamination (e.g., uncontrolled outgassing, or effluents from attitude control jets or an open cycle chemical power system). Plasmas of greatest interest (and concern) are those that are non-Maxwellian, bi-Maxwellian, drifting or otherwise have anomalous energy distributions; and the properties are time-dependent and turbulent with a multi-ion constituency and collisionality characteristics in the transition regime. It is also inevitable that magnetic field effects can not be ignored and the current flow configuration is anistropic.

These real systems represent a challenge to the theoretical community and to the experimentalist who must develop a diagnostic procedure that can contend with the multiplicity of dynamic plasma properties and apply the procedure in a manner free from unknown parasitic effects. In sections to follow, an attempt is made to identify experimental problem areas, point to existing and/or possible solutions, and illustrate the findings with specific applications to unique geoplasma domains to spaceborne systems and to laboratory-based simulation experiments. Initial emphasis will be on several aspects of basic probe diagnostics, with subsequent treatments addressing measurement demands in naturally-occurring geoplasmas, beam-plasma and vehicle-plasma interactions and in spaceborne environments affected by hollow-cathode discharges. The fundamental issues will then be carried over into discussions of larger-scale systems.

2. Fundamental Considerations and Sources of Error

2.1 Area effects

One of the oldest, most fundamental, and often overlooked considerations in probe diagnostics is the importance of reference electrode area relative to that of the diagnostic probe.[4] The Langmuir probe, like a tethered satellite, should be the smaller electrode of a two-electrode configuration with the ratio of the two areas approaching a value

which, for all practical purposes, should be considered infinite. When the two electrodes are in electrical contact with a plasma, a current will pass between them which is a function of an applied voltage difference. When the current is plotted as a function of the applied voltage difference, the resulting curve is referred to as the probe's I-V characteristic. Fig. 1 shows a schematic representation of a Langmuir probe circuit as well as a typical characteristic. (In a laboratory situation the reference electrode can, in fact, be the metal container of the plasma volume; while in spaceborne applications the reference electrode is the rocket payload or satellite skin.) The potential of the reference electrode is normally defined as zero, and it is of paramount importance to the measurement technique that this potential remain constant (with respect to the plasma potential) for all values of current. When the area of the reference electrode is sufficiently small its potential will shift, resulting in a net distortion of the probe's I-V characteristic.

From the simple considerations to be introduced here (and adapted from Ref. 4), the uncontrolled potential shift of the reference electrode is a function of the area ratio $\alpha \equiv A_r/A_p$ and the circuit current i, where A_r and A_p are the reference and probe areas, respectively. The total current collected by the probe system must equal zero, that is, $i^r = -i^p$, where i^r and i^p are net currents collected from the plasma by the reference electrode and the probe, respectively. This constraint yields the identity given by

$$i_i^r - i_e^r = -i_i^p + i_e^p, \tag{1}$$

where the subscripts i and e designate the ion and electron components of the net current. A useful view of area influences can be achieved by assuming that both electrodes are operating at potentials which are less than or equal to the plasma potential and that there are just two charged species—positive ions and negative electrons (the electrodes are therefore ion attracting). Eq. (1) can be written in the form shown in Eq. (2):

$$\alpha = \frac{\exp\chi^p - (m_e/M)^{1/2} I_i(\beta_p, \tau, \chi^p)}{(m_e/M)^{1/2} I_i(\beta_r, \tau, \chi^r) - \exp\chi^r}. \tag{2}$$

In Eq. (2), χ^p and χ^r are, respectively, the probe and reference-electrode potentials ϕ_p and ϕ_r measured with respect to the plasma potential ϕ_0 and normalized to kT_e/e [see Eq. (3)], while β_p and β_r are the corresponding radii divided by the electron Debye length λ_D [see Eq. (4)]. (Only spherical and cylindrical geometries will be considered explicitly):

$$\chi^p = e(\phi_p - \phi_0)/kT_e, \quad \chi^r = e(\phi_r - \phi_0)/kT_e, \tag{3}$$

$$\beta_p = R_p/\lambda_D, \quad \beta_r = R_r/\lambda_D. \tag{4}$$

τ is the ratio of ion-to-electron temperature T_i/T_e, m_e is the electron mass, M is the charge-normalized ion mass $M = m_i/Z^2$, where m_i and Z are the ion mass and multiplicity of ionization, and I_i is the dimensionless ion current [defined by Eq. (5)] which, in the collisionless limit, is available in numerical form in the calculations of Laframboise:[5]

$$j_i = n_e e(kT_e/2\pi M)^{1/2} I_i. \tag{5}$$

In Eqs. (2), (3) and (5) the quantities as yet undefined are the undisturbed electron density n_e, the magnitude of the charge of an electron e, the Boltzmann constant k, and the experimentally-observed ion-current density collected by an electrode j_i.

There is substantial utility in several computational results associated with Eqs. (1)-(5). The first involves the effect of area ratio on the change in reference electrode potential as a Langmuir probe is swept from its own floating potential to the plasma potential (i.e., over the entire retarding field region where the electron temperature is determined). A sample result, taken from Szuszczewicz[4], is presented in Fig. 2, where the potential χ_α^r of a cylindrical reference electrode is shown as a function of α for the case $\beta_r = 10$. The running parameter is the charge-normalized ion mass expressed in amu and the results for $\tau = 0$ and 1 are presented. χ_α^r is the value of the dimensionless potential which the reference electrode must assume in order to satisfy the identity $i^p = -i^r$ when the probe is at the plasma potential. The total shift in χ^r which results when the probe is operated over the entire transition region is given by Eq. (6) for any given set of values (β_r, τ, M, and α):

$$\Delta\chi^r = \chi_\alpha^r - \chi_f^r. \tag{6}$$

The quantities necessary for calculating $\Delta\chi^r$ are readily obtained from Fig. 2, where χ_f^r can be taken as the value of χ_α^r at $\alpha = 10^4$. As an illustration, consider the case $(\beta_r, \tau, M, \alpha) = (10, 0, 16, 100)$. In this situation $\Delta\chi^r = \chi_\alpha^r - \chi_f^r = 7.0 + 4.7 = -2.3$. This corresponds to a voltage shift of -20 V and 0.2 V for $T_e = 10^5$ and $10^{3}\,^\circ$K, respectively. Such a shift would be unknown to a probe experimenter, and the result would be an I-V characteristic that yielded a value of T_e approximately 60% higher than that actually present in the plasma.

Results like those in Fig. 2 at $\alpha = 10^4$ can be used to generate curves which present the dimensionless floating potential χ_f as a function of M for $\tau = 0$ and 1, and $\beta \leq 3, = 10, = 100$. (Here χ_f is not superscripted nor is β subscripted, since the results apply to any electrode.) The results of this approach, presented in Fig. 3, show that $-\chi_f$ increases with increasing β for a given (τ, M). This reflects the reduction in the relative sheath size for increasing values of β and consequently a reduction in the dimensionless ion current to the electrode.

Reflection on results like those shown in Figs. 2 and 3 provides some additional insight. It is first noted that errors in T_e measurements due to inappropriate values of area ratios can be kept to zero with a value of $\alpha = 10^4$. Depending on the circumstances however, that can be relaxed to values of $\alpha < 10^3$, and approach even lower limits near 10^2 for H^+ plasmas (see Ref. 4 for details).

The results of Fig. 2 can also be used to baseline considerations for two-electrode systems (including, for example, a tethered satellite), where large bias-voltages are applied. If the objective is to have the entire bias voltage applied to the smaller of the two electrodes (i.e., there is no shift in the reference electrode potential), the area ratio α must be at least 1000, and higher values are likely, depending on the plasma regime and the magnitude of the applied potential.
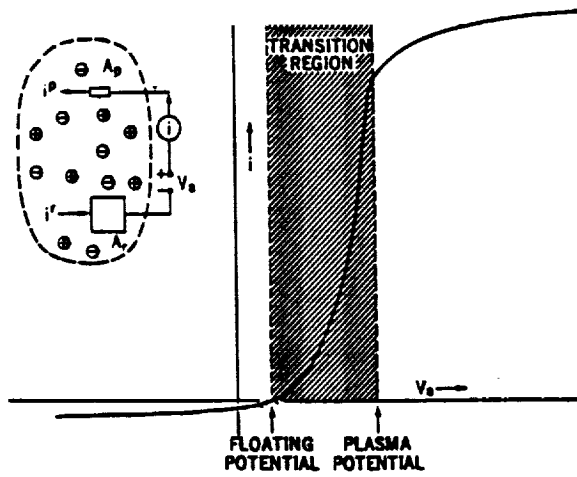
Figure 1. Schematic representation of a Langmuir-probe (or tethered satellite) circuit and a corresponding current-voltage characteristic.
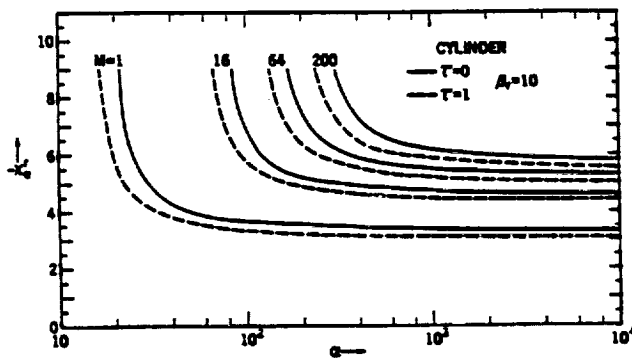
Figure 2. Dimensionless potential χ_a^r of a cylindrical reference electrode as a function of $\alpha(\equiv A_r/A_p)$ for $\beta_r(\equiv R_r/\lambda_D)$. M is the charge-normalized ion mass (in amu), $\tau = T_i/T_e$, and the Langmuir probe is assumed to be operating at the plasma potential.
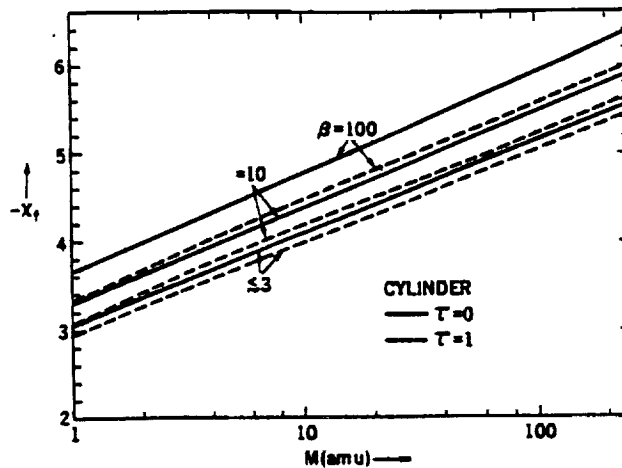
Figure 3. Dimensionless floating potential χ_f of a cylindrical body immersed in a collisionless Maxwellian plasma plotted as a function of the charge-normalized ion mass M (in amu) for ratios of ion-to-electron temperature equal to 0 and 1. β is the ratio of body radius to Debye length.

Important implications for double probe measurements of electric fields can also be extracted from Fig. 3. Such measurements are in effect high impedance determinations of the difference between the floating potentials of two probes. The assumption is that the floating potential tracks the plasma potential. That is indeed the case, but the tracking involves the local (i.e., local to each sensor) values of β, τ and M. In dynamic and irregular plasma environments, with scale sizes less than the separation distance between the double-probe sensor tips, differences between floating potentials can be mistaken as an electric field when in reality the difference can be simply a manifestation of differences in local densities, ion masses and energy distribution functions. Under such circumstances results of double probe measurements should be the subject of substantial scrutiny.

2.2 Contamination Effects

The detrimental effects of surface contamination on active electrodes in plasmas have been known for years.[6-8] Experimental studies have shown that the standard continuous-sweep approach to Langmuir probe measurements can be seriously compromised by temporal variations in the probe's effective work function. When these variations occur during the measurement interval, the current-voltage (I-V) characteristic is distorted, resulting in erroneous determinations of charged-particle densities and energy distribution functions. These effects are reviewed here, following closely the published work of Szuszczewicz and Holmes.[8]

Variations in the probe's surface condition can manifest themselves by hysteresis in the I-V characteristic when the probe is driven with a symmetric sawtooth voltage[9] (and even time function). If the I-V characteristic is not identically reproduced in the positively and negatively sloped portions of the applied sawtooth voltage [upward and downward going arrows in Fig. 4(b), respectively], the familiar hysteresis curve results. This behavior is attributed to the layering of foreign material on the surface of the probe resulting in a variation of the work function.

A model[7] for the surface layering phenomenon is illustrated in Fig. 4(a), which schematically depicts a contaminated probe in a plasma. The mechanisms for the development of the surface layer of contamination are not always easily identified but contributions may come from the deposition of sputtered material from other solids in the system or from the sorption of gases and vapors in the plasma itself. For example, a perfectly cleaned and outgassed probe when immersed in an un-ionized gas immediately begins to absorb and occlude the ambient neutral species.[10] If these species are nonconductive, an insulating layer will develop. This layer is phenomenologically represented by capacitance C_c and leakage resistance R_c in Fig. 4(a). When a plasma is part of the environment and a voltage V is applied to the probe, charged particles will flow to the probe's contaminated surface, charge up the associated capacitance C_c, and simultaneously alter the absorbate surface layer by bombardment.[11] These conditions and their associated dependence upon the applied probe voltage bring about the hysteresis in the current-voltage characteristic. [It is possible to sweep the probe voltage so slowly that the (I, V) data points come to identical equilibrium values in the up- and downlegs of the sweep.[6] In this case the measurements are still in error but

the investigator does not have the advantage of telltale hysteresis.]

When surface contamination is a problem, conventional Langmuir probes have indicated "hotter" electron distributions than actually present in the ambient medium and hotter distributions than those measured by a "clean" probe. As indicated in the discussion of Fig. 4(a), contamination can also result in an unknown offset voltage V_c across the layer, contributing to uncertainties in determining the actual voltage imposed on a plasma by fixed-potential electrodes and errors in double-probe measurements of dc electric fields. These problem areas impose genuine constraints upon experimenters and make it necessary to eliminate the contaminating species from the system or circumvent the distortions in measurement by some modification in the experimental technique. The latter approach is not always feasible, making it incumbent upon the experimenter to modify his technique so that it is not susceptible to distortion by contamination.

There are two conventional approaches which attempt to eliminate or circumvent the problem of surface contamination on Langmuir probes. One involves periodic cleaning of the probe surface by ion bombardment or heating of the probe. The second approach reduces the period of the sweep voltage to a value shorter than the time constant $\tau_c = RC_c$, where $R = R_s R_c/(R_s + R_c)$, C_c is the effective contamination capacitance, and R_s is a simple Ohmic approximation to the sheath impedance [Fig. 4(a)].

The use of a short period for the sweep voltage finds its basic limitation in values of the effective time constant $\tau_c = RC_c$. Attempts to sweep the probe voltage much shorter than τ_c have met with some success, but the fundamental limitation in τ_c can impose unworkably high sweep rates on the probe voltage. High sweep rates can often be handled in laboratory experiments, but difficulties can arise in rocket or satellite applications where data rate constraints are imposed by telemetry. At high sweep speeds and low telemetry rates, resolution of the I-V characteristic is lowered and the accuracy of measurement reduced.

The periodic probe cleaning procedure is of limited use because new contamination layers can develop immediately after the ion bombardment or heating period is ended. In the presence of high sorption rates another cleanup is sometimes necessary within seconds of the preceding cleanup termination. Consider, for example, a neutral gas environment with a 28-amu mean molecular weight at 10^{-4} Torr and a temperature of 300°K. (These parameters are typical of the ionospheric E-region at 120 km altitude.) With unity sticking probability for a clean surface and a monolayer defined by approximately 5×10^{18} molecules/m^2, the first monolayer of contamination develops in 0.13 msec. The next monolayer forms on a timescale of tens of seconds with an equilibrium surface condition resulting after some minutes.[10] This illustration clearly shows that an atomically clean surface can be a very short-lived condition.

To eliminate the aforementioned problems and to improve the reliability and versatility of Langmuir probe measurements, a pulsed plasma probe (acronym, P^3) technique[12] has been developed. The approach employs a pulsed-voltage procedure designed to maintain a single-probe surface condition throughout the collection period of the I-V characteristic; that is, it allows the existence of a contamination layer but

keeps the layer and its associated potential drop at a constant level. Fig. 5(a) shows a continuous symmetric-sawtooth sweep voltage, representing the conventional approach to Langmuir probe operation. Fig. 5(b) shows the approach of the P^3 techniques which employs a discontinuous modulated sweep of pulses following a sawtooth envelope. Between pulses, the sweep returns to a fixed baseline voltage V_B. A sequence of pulses generates distinct I-V data points for the probe's current-voltage characteristic. (Generally a single I-V characteristic is generated by 150 contiguous pulses.) During the interpulse period when the probe is at a fixed baseline voltage V_B, the current I_B collected by the probe can be monitored and used to measure variations in the probe-plasma system, and unfold density fluctuations from the I-V characteristics occurring on a short time frame in comparison to the sweep period.

The pulse sequencing procedure allows the probe to rest at its baseline potential V_B for a period of time τ_B, which is much longer than the pulse width τ_{on}. The probe current is always sampled during a subinterval within a sweep pulse, with the subinterval position and sampling duration adjusted so that the plasma is allowed to achieve a steady-state condition and all circuit transients are avoided. With τ_{on} much less than both τ_B and the time constant of the surface layer τ_c, the pulse procedure will maintain the probe's surface condition at a constant level.

In the P^3 technique the sweep time τ_s can be as long as an individual experimenter wishes since the I-V characteristic is generated by point data collected within short pulsed-voltage periods τ_{on}. The elimination of surface effects by the P^3 technique requires $\tau_{on} \ll \tau_c$, whereas in the high sweep-frequency approach it is necessary that $\tau_s \ll \tau_c$. Since τ_{on} is always much less than τ_s, the P^3 approach greatly extends the range over which the time constant effects of τ_c can be neglected. τ_{on} can be as short as the time required for the plasma to establish itself at a steady-state condition, whereas τ_s can never be that short.

This technique has proven invaluable in contaminating and highly-variable plasma environments, the most dramatic manifestation of which occurred in the pulsed-plasma-probe measurements of a reentry plasma[13] and laboratory studies of beam-plasma interactions.[14,15] Contamination problems can also be severe in diffusion-pumped vacuum systems and in spacecraft environments with effluents from attitude control jets, uncontrolled outgassing, or chemical exhaust systems. It is interesting to note that vectored nozzle expulsion of effluents can still result in substantial backflow and the deposition of contaminants on sensitive surfaces. This is illustrated in Fig. 6, which presents the results of a numerical simulation of an open-loop chemical exhaust system mounted on the end of a long, segmented cylindrical payload.[16] The effluent was taken to be 80% water and 20% hydrogen expelled in the +X direction at a rate of 53kg/sec through a supersonic (M = 4) 7° nozzle. With the effluent stagnation pressure and temperature at 1000°K and 2 atm, respectively, the resulting steady-state isodensity contours of water in mks units show a $10^{21}/m^3$ contour some 30 m in front of the nozzle and contours as high as 10^{15} in the backflow engulfing the spacecraft. This is a very high level, guaranteed to cause problems for sensitive surfaces and active plasma detectors.

2.3 Magnetic field effects

In the previous sections we have dealt with parasitic effects with potentially disastrous influences on the outcome of an experiment and on the interpretation of results. If one assumes that these effects and other sources of experimental error have been eliminated, the accuracy in one's understanding of the currents collected on a spacecraft surface and the accuracy of the diagnostic technique (probes, RPA's, electrostatic analyzers, etc.) is limited by the theoretical description of the $I - V - B$ characteristics under the prevailing plasma conditions. Most difficulty is encountered when current collection is in any one of the various transition regions, where we use the term "transition region" to describe any domain between the mathematically convenient limits of collision-free and collision-dominated, thin sheath and thick sheath, and strong field and weak field. These regions are particularly difficult to describe because one must account for detailed charge-particle trajectories that have no convenient closed mathematical form as they traverse the region between the undistrubed plasma volume and the collecting surface. In this section we look at the transition region of magnetic field effects and the associated response of cylindrical Langmuir probe electron-saturation currents. (Under certain constraints, the discussions apply to any cylindrically-shaped current-collecting body.)

Probe response in magnetoplasmas can be grouped into three broad categories defined by the relative magnitudes of the probe radius R_p, the sheath thickness ($R_s - R_p$), and the Larmor radii for electrons (R_L^e) and ions (R_L^i). We define these categories as:

$$R_p, \ (R_s - R_p) \ll R_L^{e,i} \quad \text{(weak field)}, \tag{7a}$$

$$R_p, \ (R_s - R_p) \gg R_L^{e,i} \quad \text{(strong field)}, \tag{7b}$$

and

$$R_p, \ (R_s - R_p) \approx R_L^{e,i} \quad \text{(transition field)}, \tag{7c}$$

Each of these categories has its own morphological sub-division established by the independent ratios $R_L^{e,i}/R_p$ and $R_L^{e,i}/(R_s - R_p)$. The first ratio, $R_L^{e,i}/R_p$, involves geometrical effects which result in magnetic field shadowing[17] and the associated perturbation of a fully Maxwellian plasma distribution at the sheath edge. A number of authors[3,18−21] have used this ratio to describe magnetic field effects on cylindrical probes and have shown reduced saturation currents when the ratio was small. Miller[20] and Laframboise and Rubinstein,[21] however, infer that magnetic field effects may occur even when $R_L^{e,i} \gg R_p$ if $R_L^{e,i} \lesssim (R_s - R_p)$. It is the latter inequality which is of primary concern in the present discussion.

With the use of sheath-size descriptions developed in Szuszczewicz and Takacs[22] guidelines can be determined for the enequalities (7a) - (7c) by examining the ratio $R_L^e/(R_s - R_p)$. This ratio can be written as

$$\frac{R_L^e}{R_s - R_p} = \frac{\omega_p^e/\omega_c^e}{(2.50 - 1.54\exp[-0.32R_p/\lambda_D])(e\varphi_p/kT_e)^{1/2}}, \tag{8}$$

where

$$\omega_p^e = (4\pi N e^2/m_e)^{1/2} \tag{9}$$

is the electron plasma frequency, and

$$\omega_c^e = eB/m_e c \tag{10}$$

is the electron gyro frequency.

The criteria established in (7), particularly as they apply to the effect of $R_L^e/(R_s - R_p)$ on electron-saturation currents, can now be expressed as

$$
\frac{\omega_p^e/\omega_c^e}{F(e\varphi_p/kT_e)^{1/2}}
\begin{cases}
\gg 1 & \text{weak magnetosheath}), & \text{(11a)} \\
\ll 1 & \text{strong magnetosheath}), & \text{(11b)} \\
\approx 1 & \text{transition magnetosheath}), & \text{(11c)}
\end{cases}
$$

where

$$F = 2.50 - 1.54\exp(-0.32R_p/\lambda_D). \tag{12}$$

These inequalities show that a weak-, transition-, or strong-field classification depends not only on the magnitude of the field but also on plasma parameters of density and temperature, as well as the probe size and applied potential φ_p. Thus, a 0.25 G field could have a similar effect on an ionospheric plasma sheath (typically $N_e^{max} = 10^6$ cm^{-3} and $T_e = 2000°$K at F-region altitudes) as a 30 kG field in a confined hot, dense plasma [$N_e = 5(10^{15})$cm^{-3}, $T_e = 1.16(10^7)°$K (=1 keV)]. Examining these conditions in terms of (11), we find

$$\frac{\omega_p^e/\omega_c^e}{F(e\varphi_p/kT_e)^{1/2}} = 4 \tag{13}$$

in the ionospheric case, and

$$\frac{\omega_p^e/\omega_c^e}{F(e\varphi_p/kT_e)^{1/2}} = 0.95 \tag{14}$$

for the hot, dense plasma. These results assume $e\varphi_p/kT_e = 10$ as a nominal operational value for the collection of electron-saturation currents by a cylindrical probe of radius $R_p = 3.8(10^{-2})$ cm. Since Eqs. (13) and (14) are of comparable magnitude, their results show that dramatically different probe-plasma systems can have similar classifications with regard to magnetosheath effects.

This semi-quantitative approach is helpful but far from complete since the anisotropic nature of charged-particle motion makes it necessary to consider the field direction $\hat{B}$ relative to the probe and sheath axes $\hat{L}$. The most complete work done to date in this area is that of Laframboise and Rubinstein[21] who have conducted a theoretical analysis of a cylindrical probe in a collisionless plasma, with the probe operating under
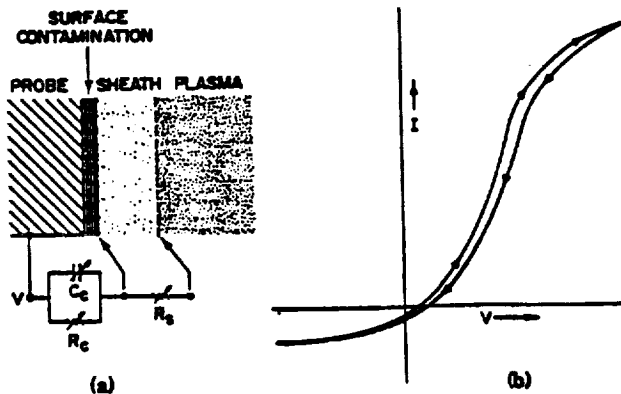
Figure 4. (a) Effective circuit equivalents in phenomenological model for surface contamination. (b) Hysteresis effects in conventional Langmuir probe current-voltage characteristic resulting from layering of surface contaminants.
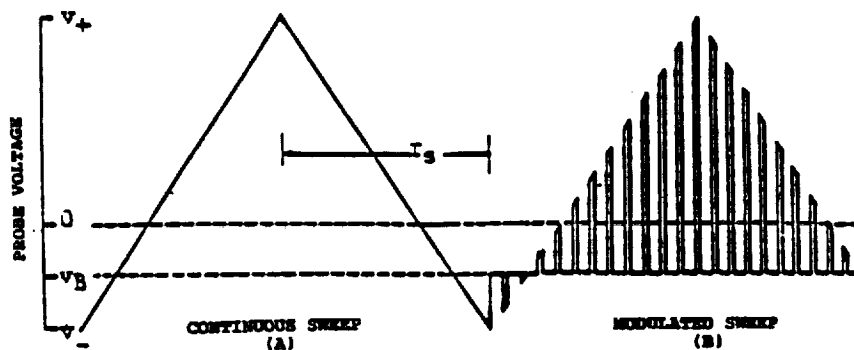
Figure 5. Continuous (conventional Langmuir probe) and pulsed-modulated (P^3 format) sweeps.

HYDROGEN EFFLUENT DENSITY CONTOURS (FMBL CODE)
BOUNDARY LAYER FLOW ONLY AT MACH 4.0 (Log #/m³)

Figure 6

98
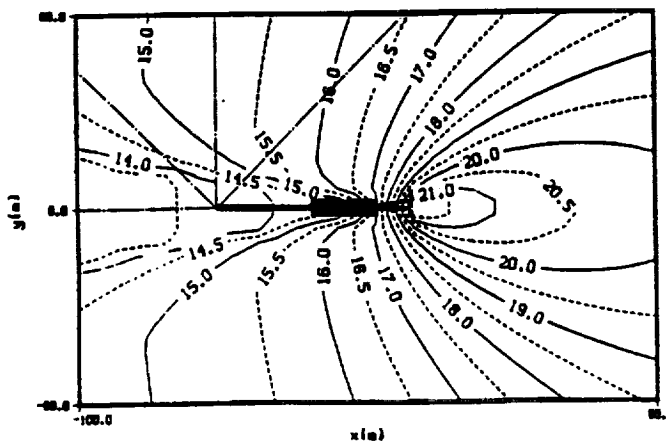
thick-sheath conditions at an arbitrary angle $\theta[\equiv \cos^{-1}(\vec{L} \cdot \vec{B}/LB)]$ with respect to a uniform magnetic field. For a probe at plasma potential, their analysis is exact; but in regions of electron saturation currents their theory provides only an upper bound and an adiabatic limit. These limits are approached, respectively, at larger and smaller values of R_L^e/L_φ, where L_φ is defined by Laframboise and Rubinstein as the gradient scale length of sheath potential $\varphi/ \mid \nabla\varphi \mid$. The adiabatic limit corresponds to $R_L^e/L_\varphi \to 0$ and can be represented approximately by $R_L^e/(R_s - R_p) \to 0$.

The influences on current-collection due to the direction of the B-field relative to the probe and sheath axes $\hat{L}$ is illustrated with rocket-borne probe data. The data was collected with a payload spinning at 4 rps and the cylindrical probe radially extended on a boom from the payload skin. The spinning payload moved probe axis from 0° to 90° with respect to the magnetic field twice during each spin period. The probe technique was that of the P^3 described in the previous section, and the baseline voltage level was set in the electron saturation region of the I-V characteristic (i.e., $I_B = I_e^{sat}$). Two major parameters varied throughout flight. The first was plasma density, making possible correlations with the contributing influences of sheath sizes; and second was the orientation of the probe axis relative to the ambient B-field. An overview of the combined effects of sheath size and magnetic field is presented in Fig. 7, where $I_B(= I_e^{sat})$ is plotted at values of I_B at $\theta = 0°({}^{+5°}_{-0°})$ and $\theta = 90°(\pm 0°)$. Using the $I_B(\theta = 90°)$ profile as the more accurate measure of relative density[20] and establishing the conversion $N_e(\text{cm})^{-3} = 1.25(10^{11})I_B(A)$, Fig. 7 demonstrates the importance of plasma density (through its control of sheath size) in determining the effect of magnetic fields on electron-current collection by cylindrical Langmuir probes. (The N_e/I_B proportionality was determined near apogee by conventional analysis[3] of the electron-saturation portion of the current-voltage characteristic, i.e., $d(I_e^{sat})^2/d\varphi_p \to N_e$. The simultaneous measurement of N_e and I_B, made possible with the P^3 technique, yielded the constant. (Sources of error identified with possible plasma depletion,[23] surface contamination,[8] reference electrode area,[4] and convective effects[2] were inconsequential.) In the ionospheric E-region trough (125-170 km), where the plasma density was lowest [$\approx 6.0(10^3)cm^{-3}$], the percent modulation, $M \equiv 100 \times [I_B(90°) - I_B(0°)]/I_B(90°) = 75\%$, was much greater than in the F region ($Z > 170$ km) where the modulation is only 10%-15%. The difference is attributed to sheath size variation since over the altitude range in this investigation the Earth's magnetic field and associated Larmor radii are approximately constant. [R_L values are constant only if temperature are constant, a situation which is not generally true over this altitude range where we can expect up to a factor of two difference. But, we can neglect the temperature effect (2×) compared to the density effect (100×).]

The results in Fig. 7 identify a problem area for plasma experimenters who utilize fixed-bias cylindrical probe measurements of electron-saturation currents to determine changes in electron density. Even when the probe is held at a fixed angle with respect to the magnetic field, the spatial or temporal profile of plasma density can be distorted by changing sheath sizes that accompany varying plasma densities. Distorted data can result in misleading interpretations of active physical principles. In Fig. 7, the

$I_B(\theta = 0°)$ curve could lead to erroneous conclusions concerning nighttime E-region depletion mechanisms (130-170 km) or applicability of the electron density gradient at the bottom-side of the F-layer (170-240 km) to the Rayleigh-Taylor instability and the triggering of ionospheric plasma irregularities.

Three cases have been selected from the ionospheric probe data in Fig. 7 to detail the behavior of $I_B(\theta)$ as a function of plasma density. The results have been normalized to $I_B(90°)$ and plotted in Fig. 8 as curves A, B, and C. We note that the modulation increases with decreasing N_e, a parametric dependence not shown in current theories involving thick sheath conditions $(R_p/\lambda_D \ll 1)$. Specifically, we find that $(\omega_p^e/\omega_c^e)/F(e\varphi_p/kT_e)^{1/2}[= R_L^e/(R_s - R_p)]$ equals 2.5, 0.47, and 0.3 for A, B, and C, respectively. In terms of the inequalities in (11), these cases qualify as transiton magnetosheath. We observe that the $R_L^e/(R_s - R_p) = 2.5$ case has the smallest modulation since it approaches the condition of weak magnetosheath. The data show that the modulation would not be zero as a result of $R_p/R_L^e \to 0$ alone. The modulation can be zero only if R_p/R_L^e and $(R_s - R_p)/R_L^e$ both go to zero, a combined condition represented by $R_L^e/(R_s - R_p) \gg 1$ [Eq. 11a] in the thick-sheath limit. The data demonstrate the important coupling of B, N_e, T_e, R_p, and φ_p in determining the degree to which magnetic fields perturb electron-current collection. One cannot give sole consideration to R_p/λ_D or R_p/R_L^e, but rather their important interrelationships as described in Eq. (11).

The consequences of these results are substantial in the following context:

1) Magnetic field effects on electron current collection characteristics can be dramatic. If strong magnetosheath conditions prevail, the use of a $B = 0$ model for I-V characteristics could lead to errors in N_e determination as big a factor as 10;

2) There is no $B \neq 0$ model available to date which describes probe current collection characteristics in the transition-magnetosheath domain. This is the domain often encountered in space plasma diagnostics.

3) The transition- and strong-magnetosheath conditions are guaranteed to prevail in analysis of currents flowing to a charged spacecraft emitting a net negative particle beam. For the charging/discharging process to be properly analyzed, the detailed controls of a superimposed magnetic field must be taken into account.

3. Measurements in Dynamic Space Plasma Environments

Thus far the treatment of current collection from plasmas has dealt with experimental and theoretical problems in plasma probe diagnostics, with perhaps an unfortunate suggestion that there is substantial difficulty in obtaining accurate information from the attendent current collection characteristics. While experimental and analytical care is warranted, there can be a wealth of valuable data in a properly implemented and analyzed experiment configuration. We attempt in this section to develop this perspective, and choose to treat an area of plasma and space plasma physics that has a focus on plasma instabilities, irregularity distributions and multi-ion constituencies. While instabilities and irregularity distributions tend to be standard fare in dynamic plasma environments, little diagnostic attention has been given to the impact of cases
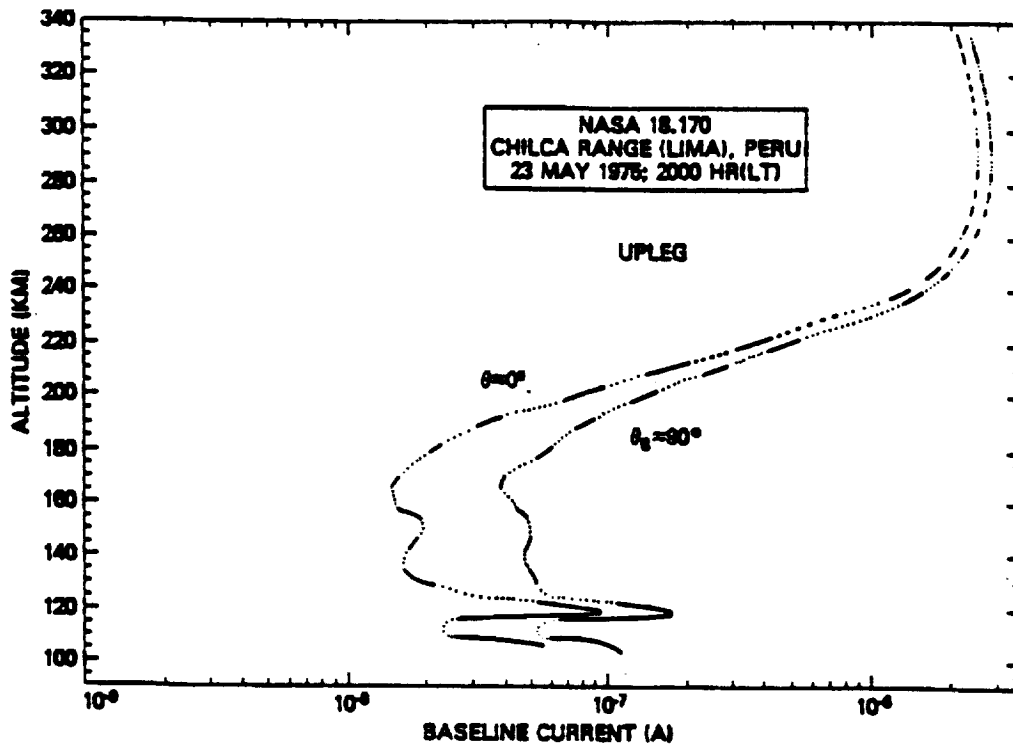
Figure 7. Baseline current I_B collected when the probe was at $0°$ $\left(^{+5°}_{-0°}\right)$ and $90°$ with respect to the geomagnetic field.

CURVE	$N_e(cm^{-3})$	R_p/λ_D	$R_L^e/(R_g - R_p)$
A	$4(10^5)$	0.11	2.5
B	$1.5(10^4)$	0.021	0.47
C	$5(10^3)$	0.012	0.30
U	—	$\ll 1$	—
L	—	$\ll 1$	—

VARYING PLASMA CONDITIONS

$e\Phi_p/kT_e = 5,$
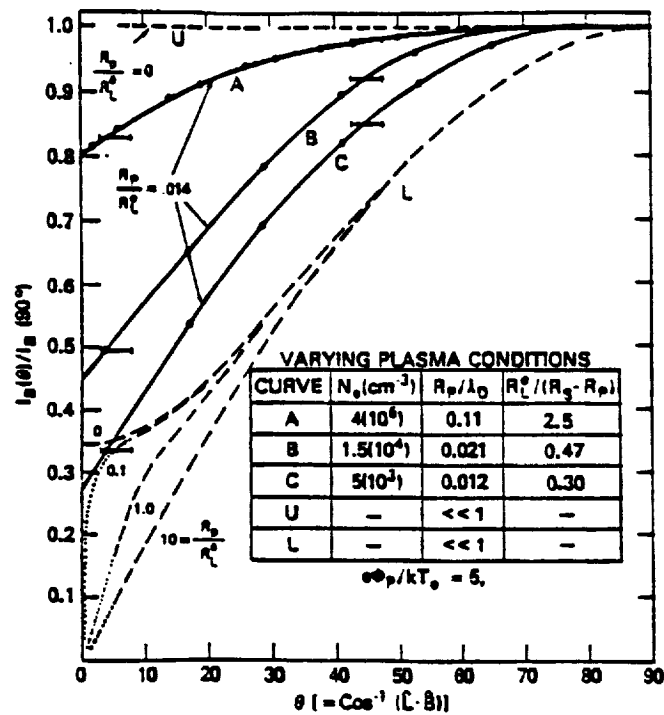
Figure 8. Experimental (curves A, B, and C) and theoretical (curves U and L with parametric dependence on R_p/R_L^e, U and L define the upper and lower bounds discovered in the text) results showing the effect of magnetic aspects on cylindrical electron-collecting probe current.

101

which involve a multi-ion population and the associated effects on the growth of the instability process and impact on irregularity scale size distributions. We develop this latter perspective here, using unique features of ion and electron current collection characteristics by Langmuir-type probes. We will do this by focussing on the S3-4 satellite experiment,[24] which was designed to explore the role of multi-ion distributions in instability processes. The treatment presented here follows that in Ref. 24.

The S3-4 experiment employed a pair of pulsed plasma probes (P^3), each of which was capable of simultaneous measurements of electron density, temperature and density fluctuation power spectra, regardless of the state of turbulence or the degree of irregularity in the ionospheric plasma medium. Together, the pair of probes also provided mean-ion-mass fluctuation measurements to a maximum Nyquist frequency of 200 Hz.

Subject to the selection of one of eight commandable modes of operation, each of the probes had applied to it some variation of the voltage function illustrated in Fig. 5. The pulse modulated waveform, following the sawtooth envelope, provided the fundamental data set for a "conventional" Langmuir current-voltage characteristic and associated determination of N_e and T_e (Chen[3]) at a nominal 3 Hz rate. During the interpulse period, a fixed-voltage V_B was applied to the probe and associated current measurements provided a running measure of density fluctuations (assuming $\delta I_B \propto \delta N_e$) and a time-dependent data set for power spectral analysis with a Nyquist frequency of 400 Hz in the high data-rate mode.

The probes were routinely operated with V_B on one probe set for electron-saturation-current collection (defined as the E-probe with $I_B = I_e(\text{sat}) \equiv E$), while the value of V_B on the second probe was biased for ion saturation current collection (defined as the I-probe with $I_B = I_i(\text{sat}) \equiv I$). The expressions for the currents collected by the two cylindrical probes take the forms

$$E \equiv I_e(\text{sat}) = N_e \sqrt{\frac{kT_e}{2\pi M_e}} \, A_p e \left\{ \frac{2}{\sqrt{\pi}} \left(1 + \frac{e\phi_p^e}{kT_e} \right)^{1/2} \right\} \tag{15}$$

(Chen[3]; for thick sheaths), and

$$I \equiv I_i(\text{sat}) = N_i \sqrt{\frac{kT_i}{2\pi M_i}} \, A_p e \left\{ \frac{2}{\sqrt{\pi}} \left(\frac{|e\phi_p^i|}{kT_i} + \frac{M_i w^2}{2kT_i} \right)^{1/2} \right\} \tag{16}$$

(Hoegy and Wharton,[26] for probe axis perpendicular to the vehicle velocity vector in the ionospheric plasma rest frame). In the above equations, A_p is the probe area, $M_{e(i)}$ and $N_{e(i)}$ are the mass and density of the electron (ion) population, $T_{e(i)}$ is the associated temperature of an assumed Maxwellian distribution, e is the fundamental electron charge, k is Boltzmann's constant, w is the satellite velocity, and $\phi_p^{e(i)}$ is the baseline voltage V_B applied to the $E(I)$ probe and referenced to the plasma potential ($\phi_p^{e(i)} = V_B^{e(i)} - V_\infty$).

The square of the ratio $I_e(\text{sat})/I_i(\text{sat})$ can be written as

$$\left(\frac{I_e(\text{sat})}{I_i(\text{sat})}\right)^2 \equiv \left(\frac{E}{I}\right)^2 = \frac{T_e}{T_i}\frac{M_i}{M_e}\left\{\frac{1+\mid e\phi_p^e/kT_e\mid}{(M_iw^2/2kT_i+\mid e\phi_p^i/kT_i\mid)}\right\} \qquad (17)$$

with additional manipulation (assuming $\mid e\phi_p^e\mid \gg kT_e$) resulting in

$$\left(\frac{I_e(\text{sat})}{I_i(\text{sat})}\right)^2 = \frac{M_i}{M_e}\left|\frac{\phi_p^e}{\phi_p^i}\right|, \qquad\qquad \frac{1}{2}M_iw^2 \ll e\phi_p^i; \qquad (18a)$$

$$\left(\frac{I_e(\text{sat})}{I_i(\text{sat})}\right)^2 = \frac{2\left|e\phi_p^e\right|}{M_ew^2}, \qquad\qquad \frac{1}{2}M_iw^2 \gg e\phi_p^i; \qquad (18b)$$

$$\left(\frac{I_e(\text{sat})}{I_i(\text{sat})}\right)^2 = \frac{M_i}{M_e}\left|\frac{\phi_p^e}{\phi_p^i}\right|\left(1+\frac{M_iw^2}{2e\phi_p^i}\right)^{-1}, \quad \frac{1}{2}M_iw^2 \approx e\phi_p^i. \qquad (18c)$$

For laboratory and rocket-borne experiments Eq. (18a) would apply, whereas in the S3-4 satellite investigation, Eq. (18c) applies. Eq. (18c) is plotted in Fig. 9 for two sets of bias potentials, $(\mid\phi_p^e\mid,\mid\phi_p^i\mid) = (2V, 1V)$ and $(1V, 2V)$. The results in Fig. 9 show that over limited mass ranges (e.g., 1-4, 4-8, 16-32 amu), variations in $(I_e/I_i)^2$ can be taken to vary directly with ion mass for constant values of ϕ_p^e and ϕ_p^i.

Bulk processing and plotting of $P^3/S3-4$ data included orbit-by-orbit plots of relative electron density as measured by changes in ion- and electron-saturation currents near the F-region peak. (This is the region for minimum sheaths in ionospheric Langmuir probe operations.) A representative sample of this data collected on orbit 2177 is shown in Fig. 10, where the abscissa coordinates are universal time, altitude, latitude, longitude, magnetic latitude, and L-shell value. The probes magnetic aspect angle is also plotted in the figure.

The left-hand edge in Fig. 10 corresponds to the satellite's ascending node (south-to-north) in the midnight hemisphere near the south magnetic pole. With increasing time (UT) the satellite passed through the nighttime equator, the main trough, over the northern auroral oval and into the dayside ionosphere where vehicle solar cell voltage biased the entire vehicle such that both probes drew approximately equal ion-saturation currents. (It is worthwhile to note that the shifted payload potential was a direct consequence of the area ratio issue discussed in Section 2.1.)

The simultaneous measurements of electron- and ion-saturation currents, $I_B(E)$ and $I_B(I)$, respectively, provide confidence that the observed irregularities involve plasma variations and not just secondary effects (e.g., aspect sensitivities or variations in spacecraft potential).

While data sets like that shown in Fig. 10 provided global maps of large scale ionospheric features, primary investigative objectives were directed at the relationships
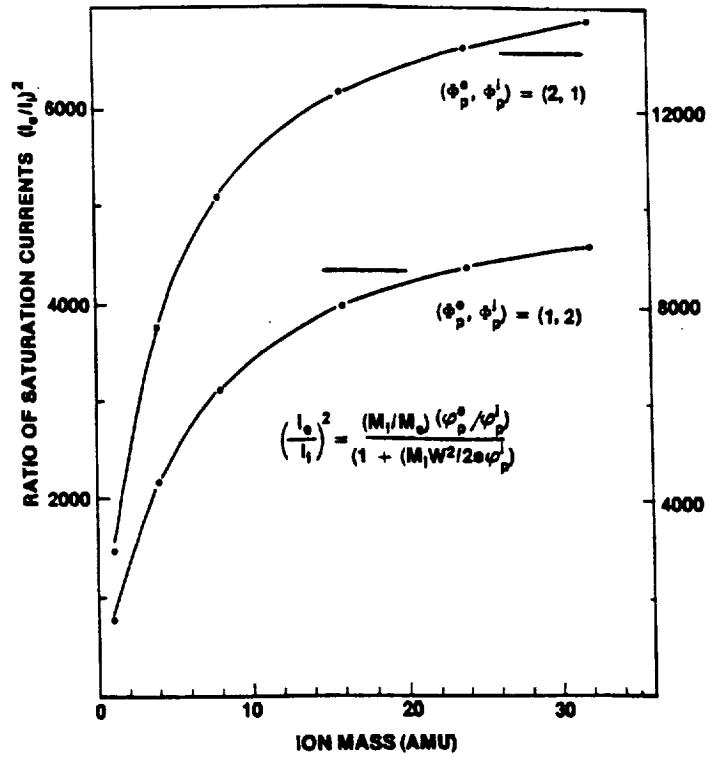
Figure 9. Dependence of the saturation current ratio $(I_e/I_i)^2$ on ion mass.
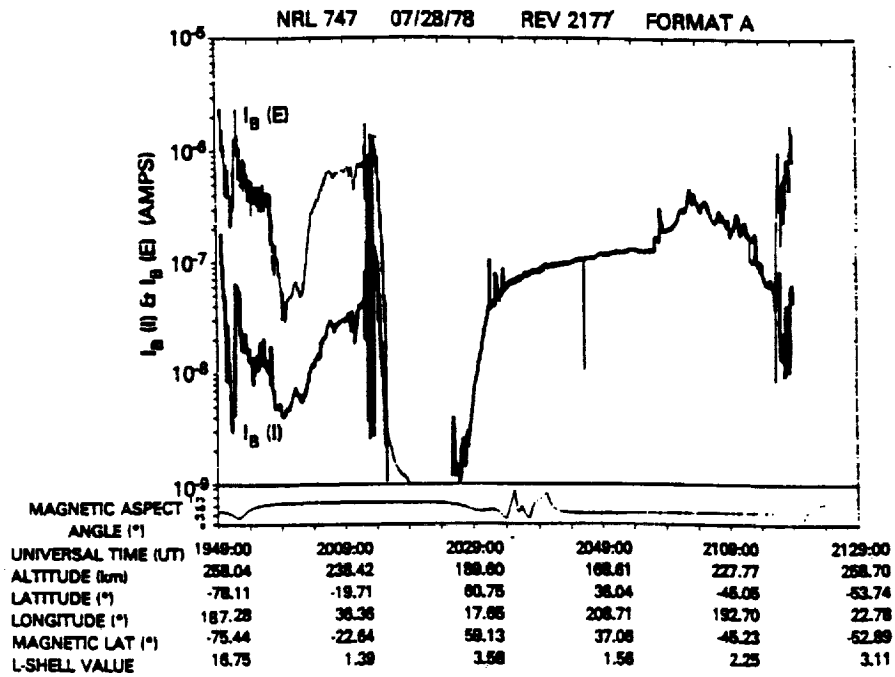
Figure 10. Relative electron density as measured on one complete orbit by the pulsed-plasma-probe experiment on the S3-4 satellite.

between the large scale features and much smaller scale irregularities (tens of meters and less) believed to result from multi-stepped plasma processes. To this end, the fundamental data sets $I_e(\text{sat})$ and $(I_e(\text{sat})/I_i(\text{sat}))^2$ were Fast-Fourier analyzed to determine density and ion-mass fluctuation power spectra $P_N(k)$ and $P_M(k)$, respectively, were

$$\left| \frac{\delta I_e}{\bar{I}_e} \right|^2 \equiv \left| \frac{\delta N_e}{\bar{N}_e} \right|^2 \rightarrow P_N(k) \tag{19}$$

and

$$\frac{\delta(I_e/I_i)^2}{(\bar{I}_e/I_i)^2} \equiv \frac{\delta M_i}{\bar{M}_i} \rightarrow P_M(k). \tag{20}$$

The anaytical relationship between $\delta N_e/\bar{N}_e$ and $\delta M_i/\bar{M}_i$ can be simply established for a 2-component ion distribution of masses and densities (M_α, M_β) and (N_α, N_β), respectively. This is done by using the definitions

$$\bar{M}_i = \frac{M_\alpha N_\alpha + M_\beta N_\beta}{(N_\alpha + N_\beta)}, \tag{21a}$$

$$N_e = N_\alpha + N_\beta, \tag{21b}$$

$$N_\alpha = N_\alpha^0 + N_\alpha^1, \tag{21c}$$

$$N_\beta = N_\beta^0 + N_\beta^1, \tag{21d}$$

$$\delta N_e = \delta N_\alpha + \delta N_\beta = N_\alpha^1 + N_\beta^1; \tag{21e}$$

and a straightforward manipulation to derive

$$\frac{\delta M_i}{\bar{M}_i} = \frac{\delta N_e}{\bar{N}_e} \, f(\alpha, \beta), \tag{22a}$$

where

$$f(\alpha, \beta) = \left\{ \frac{\left(\frac{M_\alpha}{M_\beta} \right) - 1}{\left(\frac{M_\alpha}{M_\beta} \right) \left(\frac{N_\alpha^0}{N_\beta^0} \right) + 1} \right\} \left\{ \frac{N_\alpha^1/N_\beta^1 - N_\alpha^0/N_\beta^0}{(N_\alpha^1/N_\beta^1) + 1} \right\}. \tag{22b}$$

It is appropriate to note that the experimental determination of mean-ion-mass fluctuations $\delta M_i(\rightarrow P_M)$, through variations in $[I_e(\text{sat})/I_i(\text{sat})]^2$, assumes the relative constancy of all potentials. (This includes the spacecraft potential as well as the potentials which each probe presents to the plasma.) The spacecraft potential can vary as a direct result of changes in local plasma density, since the floating potential of a body is dependent upon the ratio of its radius to the local Debye length. For large space vehicles however, floating potential variations caused by even substantial plasma density variations should be small.[4] Another possible source of potential variations involves charging of contamination layers on the vehicle and/or on the probes.[8] From the S3-4 data, variations in $(I_e/I_i)^2$ associated with charging on contamination layers appear to be a slowly varying function of time with no attendant effects on P_M. Therefore,

it has been concluded that the spectral dependence of P_M is indeed representative of variations in mean-ion-mass δM_i.

To experimentally demonstrate $P_M(k)$ and the associated relationship, with $P_N(k)$ consider the high-resolution measurements (rev. #2123) of the relative electron density across the nighttime equator (Fig. 11). The peak electron density is approximately $5 \times (10^5)$ cm^{-3} at $I_B = 3 \times (10^{-6})$ amp. The large scale depletions are seen to extend to two orders of magnitude with widths ranging from 50 to 170 km over a 600 km orbital segment.

P_N and P_M results are presented in Fig. 12 for a one second interval located by point A in the density profile of Fig. 11. Fitting the results to a power law behavior shows

$$P_N = A_n f^{-2.9} \tag{23a}$$

and

$$P_M = A_m f^{-1.5}. \tag{23b}$$

By assuming that the time (frequency) domain spectral analysis in Fig. 12 can be converted to wavelength through the vehicle velocity (7.53 km s^{-1}), the experiment shows $f_N^{-2.9}(\propto k^{-2.9})$ from $k \approx 2\pi/1$km to $k = 2\pi/20$m. This is the first such satellite determination to wavelengths as short as 20m, with the earlier work of McClure and Hanson[26] having defined some of the spectral features of equatorial spread-F down to 70m. (Conversion to the component of k perpendicular to the geomagnetic field extends the low wavelength end of Fig. 12 down to $k = 2\pi/6$m, the approximate value for O$^+$ Larmor radius.)

The spectral index for P_N is approximately 15% steeper than previously reported values[27] for conditions of bottomside spread-F, but well within the distribution of S3-4 spectral indices currently being accumulated and analyzed for conditions indentified with the intermediate wavelength domain ($k = 2\pi/1$ km to $k = 2\pi/20$m).

The $P_M \propto f^{-1.5}$ observations are the first of their kind and unique to the P^3/S3-4 experiment. Currently there are no computational guidelines on the expected behavior, but there is sufficient evidence in laboratory plasma studies to warrant such systematic considerations of ions and their role in the hierarchy of possible mechanisms covering the spectrum of observed ionospheric irregularities. The importance of ions is clear...even from the simple considerations of the Rayleigh-Taylor instability in which a difference in charged-particle drift velocities produces an electric field across a horizontal perturbation. There drift velocities are mass dependent ($\bar{V}_i \propto M_i(\bar{g} \times \bar{B})/B^2$) and vary directly as the mass of the ith species. Similar mass discriminatory effects play an important role in ambipolar diffusion processes across gradients in plasma density. The process operates more rapidly on lighter ions and can result in "patches" of varying ion mass, with local variations in conductivity and electric fields, and ultimately an ion-dependent interaction in the process of energy dissipation in the large-to-small
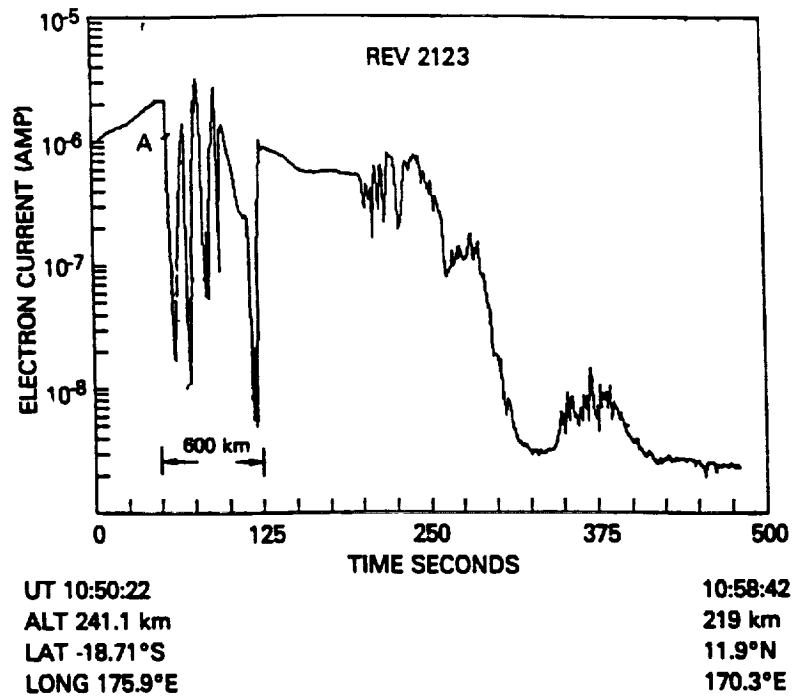
Figure 11. An expanded view of relative electron density encountered during the nighttime equatorial crossing on S3-4 rev 2123. The relative electron density is presented by baseline electron saturation current.
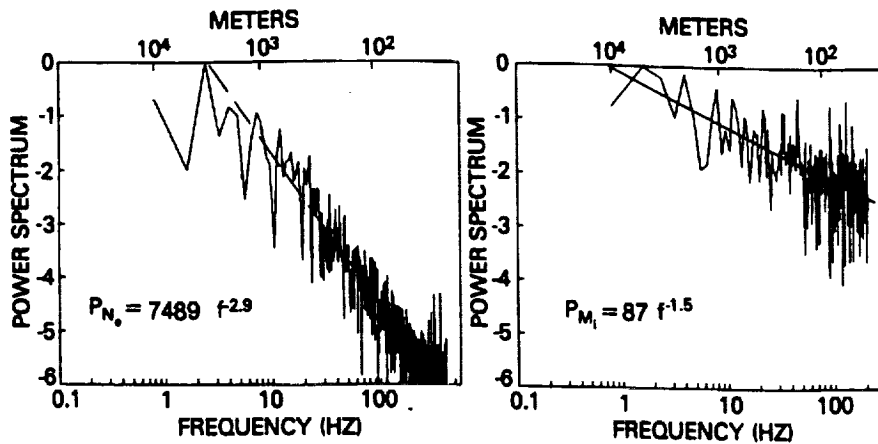
Figure 12. Sample illustration of simultaneously determined density fluctuation power spectrum P_N and mean ion mass fluctuation power specturm P_M.

scale irregularity distribution. The P_M measurement has been designed to test for just that type of interactive mode. $\delta M_i / \vec{M}_i$ is a fairly complicated function of M_α / M_β, N_α^0 / N_β^0, N_α^1 / N_β^1 and $\delta N_e / \vec{N}_e$ itself [see Eq. (22)]; and at this point we can only speculate on the many manifestations that P_N and P_M might take for the varied ionospheric conditions encountered in the S3-4 mission. For example, it has been suggested that differences in gradient scale lengths for N_e and $M_{\alpha,\beta}$ would result in a more rapid fall off with increasing k for the quantity with an initially larger gradient scale length. This difference should be a direct observable through the P_N and P_M determination. Furthermore, there is the possibility that the simultaneous measurement of $P_M(k)$ could help differentiate between a k^{-2} spectrum due to sharp edges and a k^{-2} spectrum due to gradient-drift or drift-dissipative waves.

4. Currents in Future Space Plasma Experiments

4.1 Tethers, Uncontrolled Potentials and Plasma Contactors

Thus far the treatment has focused on the experimental implementation, collection and analysis of currents to probe systems. We transition now to larger systems like spacecraft and tethers, and note that while bigger systems appear to grow more complex, the issues in many ways remain the same...currents, sheaths and fields. We also note that probes will play important roles in diagnosing the currents and their controls in the larger systems.

We now address several of the larger systems and look not only into sheath currents, and currents collected on spacecraft surfaces, but we look into the effects of large potentials and current closure through the ionosphere. This additional aspect is addressed because many mission concepts advanced in the planning of tethered satellite systems (TSS), beam experiments and Space Station applications are faced with uncertainties in current closure in the ionosphere and the threat of uncontrolled potentials.[28-30] The problem of large and uncontrolled potentials was the subject of a special TSS-1 report that pointed out that tether-system potentials could reach hundreds to thousands of volts depending on the nature of operating anomalies and the tether deployment distance.

A continuing effort has been made to develop techniques with the ability to control these large potentials and maintain spacecraft (and tethered satellites) at or near the local plasma potential. Some success has resulted from improvements in vehicle surface conductivities and expanded areas for ionospheric current collection; but the magnitude of the problem has brought about a focus on the application of high-current on-board charged-particle sources, often referred to as "plasma contactors" or "plasma bridges."[29-33] This was one of the recommendations of the TSS-1 committee on charging.[34] With this result and the call for innovative technologies in space, plasma contactors are now expected to play an additional role in electrodynamic tether applications to power and thrust generation on the Space Station. These applications exploit the stable self-orientation of a long tether (see Fig. 13) along with associated Faraday $(\vec{V} \times \vec{B}) \cdot \vec{L}$ voltages and $\vec{I} \times \vec{B}$ Lorentz forces, where $\vec{V}, \vec{L}$ and $\vec{I}$ are the velocity, length and current in the tether, and $\vec{B}$ is the geomagnetic field. The current-

Figure 13. A) Potential diagram for tether as a generator, (load at bottom, tether deployed upwards), and B) as a thruster (with power supply at bottom, tether deployed upwards). From Hastings and Martinez-Sanchez.[35]

carrying capabilities of the tether depend on the emf (induced in the generator mode or provided by an on-board power supply in the thruster mode), its impedance and the effectiveness of the ionospheric path to complete the circuit. A 20 km aluminum cable several mm in diameter would have an impedance $\approx 10 - 50\Omega$, and in principle could carry a self-induced short-circuit current of 100A [Hastings and Martinez[35]]. However, maximum ionospheric currents ($n_e^{max} \sim 10^6 cm^{-3}$) can only provide ~ 10 ma/m^2, so to draw even 10A of ionospheric current would require 1000m^2 of collecting surface. In this case, plasma contactors are seen as a solution. Their high density plasma clouds hold promise for enhanced local plasma conductivities, larger effective collecting areas, and reduced threat of uncontrolled potentials. In its final report, the TSS-1 charging committee recommended the inclusion of a hollow-cathode in its mission.[34]

One type of plasma contactor is the hollow-cathode discharge, illustrated schematically in Fig. 14A. Fundamentally, it is a thermionic electron emitter in the presence of a high gas flow, which can produce plasma densities upwards of 10^{14} cm^{-3} near the cathode orifice.[36-38] The expansion characteristics of this plasma (and its associated "contactor" capabilities) are influenced by specific device-design considerations, the ambient plasma itself, and the local geomagnetic field. The ideal contactor should provide large controllable currents of electrons and ions at minimum applied fields in the cathode-anode region. We note, however, that large controllable currents are best carried by electrons, provided they can move freely not only parallel but perpendicular to magnetic fields. The latter condition requires that $\nu_e > \Omega_e$, where ν_e is the effective electron momentum collision frequency and Ω_e is the electron cyclotron frequency. Under normal operating conditions, particle-particle collisions are insufficient and only an "anomalous" collision term through wave-particle interactions can provide the necessary random walk process which can transport electrons perpendicular to $\vec{B}$ (note R_L^e, the electron gyroradius, is typically ~ 3 cm in ionospheric applications). Indeed, as a current source between a space platform and the background ionosphere, the HC is potentially replete with current-driven instabilities and associated wave spectra. Candidates include lower-hybrid-drift, ion-acoustic and Buneman instabilities[30,39] to name just a few. But while the bulk current-carrying characteristics of the HCD have been receiving attention, there has been little-to-no effective experimental work focussed on the wave- and wave-particle processes intrinsic to HC operations and to the physics of HC plasma interactions with the local ionospheric plasma and the geomagnetic field. These interactions are critical to device performance and to the perturbations that the device is likely to introduce in its near-space and flux-tube-coupled domains. This "plasma noise" aspect of operations due to unstable plasma modes can have serious implications for a broad range of "in situ" requirements for plasma-particle and wave measurements intended for Space Station, TSS and active particle-beam platforms.

Fig. 14A presents a schematic view of the phenomenological domains of hollow-cathode operation in a space plasma environment. The cathode can be biased in either polarity with respect to the spacecraft ground and its outer skin (assumed a conductor in contact with the ambient geoplasma). The skin will itself be of either polarity relative to the local plasma potential, and ionospheric currents will flow across the spacecraft-associated sheath. The magnitude and polarity of skin potential relative

PHENOMENOLOGICAL DOMAINS OF HOLLOW-CATHODE PLASMA INTERACTIONS
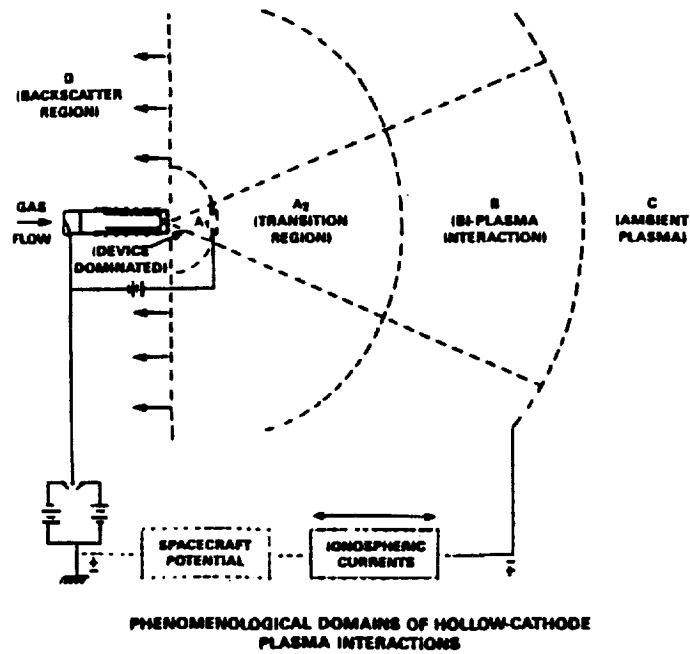
Figure 14A. Current paths and plasma domains in the hollow-cathode circuit coupling the spacecraft with the background ionosphere. (From Szuszczewicz [1985] and Szuszczewicz et al. [1988])
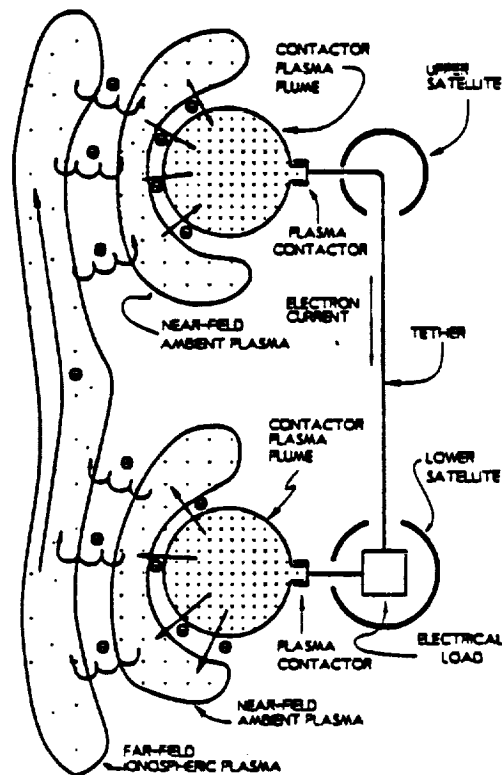
Figure 14B. Conceptualized electrodynamic tether circuit (adapted from Williams and Wilbur[45]; note that the lower plasma contactor is in an electron emitting mode so that the lower contactor can be replaced by an electron gun.

111

to space will depend on ambient plasma conditions, the spacecraft geometry and configuration, and the operation of on-board experiments (e.g. particle-beam injection). Another current path to the payload (besides that through the spacecraft sheath) is along and through the expanding hollow-cathode plasma. The expansion process, represented phenomenologically by regions A_1, A_2, B, and D, governs the current carrying capabilities of the HC. In a tethered configuration analogous to Fig. 13, the ground plane (spacecraft skin) in Fig. 14A and its current path to the ionosphere through its sheath are replaced by another hollow-cathode with its own phenomenological regions designated by A_1, A_2, B and D and its current path through the ionosphere. This is illustrated in Fig. 14B.

The plasma production and expansion process begins with neutral gas flow (typically Ar or Xe) into the cathode at pressures typically in the range 1-100 torr. Plasma is created inside the thermionically-electron-emitting cathode and the neutral gas and plasma experience a choked flow as they pass through the cathode's exit orifice (diameter ≈ 0.030") into domain A_1. In this phenomenological model, A_1 is defined as the "Device Dominated Region" because the attendant plasma processes depend on the cathode characteristics and the anode-to-cathode fields. In zero order, the expansion of the neutrals in A_1 is thermal, while that of the charged particles is thermal with increasing drift velocities imparted by the applied field. The domain is collisional, with orifice plasma and neutral densities quoted at 10^{15} and 10^{17} cm^{-3}, respectively (J. McCoy, private communication). The field in region A_1 can impart a relative drift velocity between the electrons and ions, with the electrons easily satisfying the Dricer field condition for the onset of collective plasma effects and the Buneman instability.[30,40−42] This instability can turn on and off, heating the electron population and destroying all assumptions of isothermality. This will affect the plasma resistivity and the current delivery capabilities of the device.

Exiting A_1, the source plasma can diminish to levels near 10^{12} cm^{-3} where it begins its exposure to a new electric field configuration resulting from the potential difference between the anode and the ambient plasma (beyond the sheath edge in region C). Region A_2 is dominated by the source plasma, which by current estimates should have a high kinetic β, excluding the ionospheric plasma and the geomagnetic field. A_2 is a transition region in which the source plasma diminishes in dominance over the domain and its kinetic β drops to unity. This is expected to occur over one-to-several meters, depending on prevailing conditions.

The processes in Regions A_1 and A_2 may be considered less complex than those in Region B, where counterstreaming source and ionospheric plasmas and magnetic field effects must be taken into account. In Region B, the magnetic fields control the net electron emission or collection characteristics of the contactor, and it is here that the payload is truly in "contact" with the ionospheric plasma through the HCD. While it is the physics in this region that holds the key to the capabilities of the device to deliver or attract large currents with low-to-moderate anode potentials, the properties of the expanding hollow-cathode plasma in region A_2 and that of the ambient ionosphere in C define the zero-order inputs for the interactions which form the basis of current flow.

The final input control involves the magnitude of the ambient magnetic field and its orientation relative to the cathode axis and the plasma "surfaces" defining Region B.

Since the introduction of the phenomenological model of HC plasma interaction domains by Szuszczewicz,[30] there has been a number of theoretical[43,44] and experimental[45-48] efforts focussed on their existence and controls. Region B, for example, has been referred to by Davis et al.[43] and Williams and Wilbur[45] as a "double sheath" or a "double layer," across which most of the potential between the HC and ambient plasmas is dropped, and where the HC and background plasma counterstream.

The regimes A-D in the hollow-cathode plasma represent only one subelement in the current closure path illlustrated in Figs. 14A and B. Other subelements include the ionospheric path itself, and the return current path through the reference electrode (or tethered satellite) sheath. To understand, measure and model the current closure system and to establish the I-V-B characteristic is indeed a challenge. There are some guidelines from laboratory simulation experiments, but while they represent valuable adjuncts to the development of theoretical models and the planning of space-flight investigations, care must be taken in their interpretation and their extrapolation to direct applications on a space platform. This is not to say that there is not a history of meaningful laboratory simulations of space plasma processes, even when scaling laws did not rigorously apply. We include in this class the reconnection and tether-simulation experiments of Stenzel et al.[49-51] and Urretia and Stenzel[52], as well as the energetic beam-plasma-discharge studies of Bernstein et al.[53-55], Szuszczewicz et al.[56-57] and Kellogg et al.[58-59] In the case of HC simulations there are some special problems however, and we illustrate that with reference to Table 1 where we compare the HC and background plasma properties that are likely to be encountered in space with those that have been encountered in the lab. Several problem areas stand out. If we look first at the ratio of hollow-cathode plasma density N_{HC} to that of the background plasma N_O to which it must couple, we see a major discrepancy....$N_{HC}/N_O = 2.8$ under laboratory conditions compares unfavorably with projected spaceflight applications where we expect $48 \leq N_{HC}/N_O < 1.9(10)^5$. Differences between laboratory and spaceflight conditions also include relative thermal energy densities (2.2 in the lab and 7400 in space) and the diamagnetic properties of the plasmas (expressed by $\beta = 8\pi N_{HC}(kT+K.E.)/B^2 = 0.15$ and 3.7 in the lab and in space, respectively). (The difference in the β-values stems from the directed velocity of the space vehicle relative the background plasma, a value near 8 km/sec on a low-earth-orbiting spacecraft and in the range 0.5-2.0 km/sec on a rocket.)

Other problems involve the laboratory simulation of the background ionospheric plasma, which should be fully-Maxwellian with $T_e = 0.2$ eV. Instead, we find in the work of Williams and Wilbur[45] a two-component electron distribution (defined by T_e^c and T_e^h) in the background simulator. The temperatures of the cold and hot components (T_e^c and T_e^h) were at 6.5 and 52 eV, respectively, and their relative densities N_o^h/N_o^c were at a 4% level. With plasma interaction processes critically-dependent on relative energies and densities, and the specifics of the energy distribution functions of the interacting plasmas, it is clear that the laboratory experiments conducted to date must

Table 1

COMPARISONS OF HOLLOW-CATHODE AND BACKGROUND PLASMA REGIMES

	Lab Simulation [After Williams and Wilbur[59]]	Typical Space Application
Plasma Densities		
Hollow-Cathode Plasma Density,* N_{HC}	$1.9\,(10^8)cm^{-3}$	$1.9\,(10^8)cm^{-3}$
Background Plasma Density, N_o	$6.8\,(10^7)cm^{-3}$	$10^3 < N_o \le 4(10^6)\,cm^{-3}$
Ratio N_{HC}/N_o	2.8	$48 \le N_{HC}/N_o < 1.9(10^5)$
Plasma Electron Energies		
Hollow Cathode Plasma	Multi-Component $T_e^c \sim 4.8eV$, $T_e^h \sim 45eV$	Multi-Component** $T_e^c \sim 5eV$, $T_e^h \sim 50eV$
Background Plasma	Multi-Component $T_e^c \sim 6.5eV$, $T_e^h \sim 52eV$ ($N_o^h/N_o^c = 4\%$)	Single-Component Maxwellian $T_e \sim 0.2eV$ ($N_o^h/N_o^c = 0$)
Relative Thermal Energy Densities		
$N_{HC}kT_e^c/N_o kT_o^c$	2.2	7.4 (10^3)
Hollow-Cathode β		
$\beta = 8\pi N_{HC}(kT + K.E.)/B^2$	0.15	3.7

* These values depend on operating parameters and point of measurement. We use here the published values of Williams and Wilbur[59] and assume the same values apply in a spaceborne system.

** We assume the multi-component nature observed in the lab will also apply in space.

114

be carefully scrutinized before their results are directly extrapolated to spaceborne applications. There is no question however that there is merit in the accumulated results, for Williams and Wilbur[45] and Vannaroni et al.[46] have drawn attention to the non-Maxwellian nature of the hollow-cathode plasma and have helped develop an appreciation for the expansion process and interacting plasma regimes illustrated in Figures 14A. They have established a database that needs to be tested and explored in space.

The relative merits and limitations of individual laboratory experiments notwithstanding, we turn now to the power spectral density measurement of electrostatic waves in the investigation of Szuszczewicz et al.[60] Shown in Fig. 15, these measurements were taken in a 1m x 2m chamber with the hollow-cathode mounted on one end of the system and allowed to expand into vacuum. The experiment was designed to test the original position of Szuszczewicz,[30] that the hollow-cathode plasma was an intrinsically "noisy" device with significant potential for perturbing spaceborne experiments designed to study other plasma phenomena. The experiment was effectively a survey of wave observations with parametric control over hollow-cathode conditions (current, voltage and gas flow) and superimposed magnetic fields. Wave structures were ubiquitous, ranging from intense lower frequency white noise characteristics like that shown in Fig. 15A (levels at volts/meter) to mv/meter levels shown in Fig. 15B. (Note that the high power spectral component at the low frequency end in Fig. 15B is the 120 Hz multiple of the ac power.) In panels C and D we see varying waveforms and spectral indices with and without resonances in the 0.01 - 2.0 Mhz region. The overwhelming conclusion is that hollow-cathode plasmas are replete with wave perturbations driven by current and streaming instabilities, with important effects on energy distribution functions and net current carrying capabilities. Certain modes appear innocuous (e.g. mv/m E-field fluctuations) while others appear to generate large perturbations (e.g. volts/m).

The results of Williams and Wibur,[45] Paterson et al.,[47] Vannaroni et al.,[46] and Szuszczewicz et al.,[60] while limited in the integrity of their capabilities to simulate HC operations in space, provide powerful guidelines for future experiments and establish the clear need for a spaceborne experiment to test and characterize the principles and operations of the hollow-cathode device and develop a detailed understanding of the I-V-B characteristics. These I-V-B characteristics represent the complete system of current closure with all the complications discussed in Sections 1-3. There will be bi-Maxwellian and non-Maxwellian energy distributions, multi-ion constituencies (e.g., Ar^+ or Xe^+ from the hollow cathode device, and O^+, NO^+, O_2^+ from the background plasma), and a broad spectrum of turbulence as suggested in the results of Figure 15. There will also be the challenge of properly diagnosing the currents impinging on the tethered satellite. Should there still be large sheaths and potentials there will surely be anomolous energy distributions and anisotropies in the charged particle populations. Some perspectives on these phenomena will be advanced in the next section.

4.2 Beams, Charging and Return Current Measurements

Current closure involving plasmas and man-made systems like probes and satellites
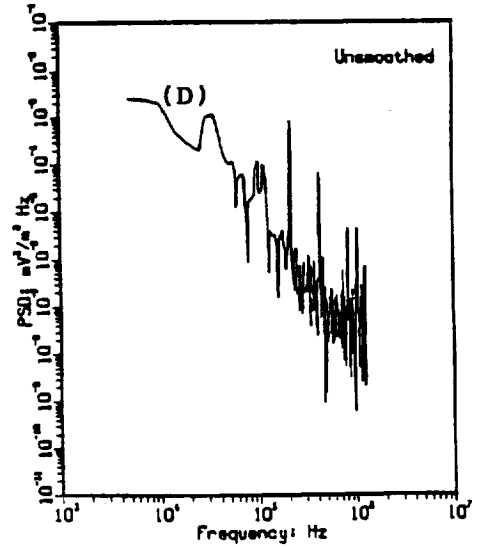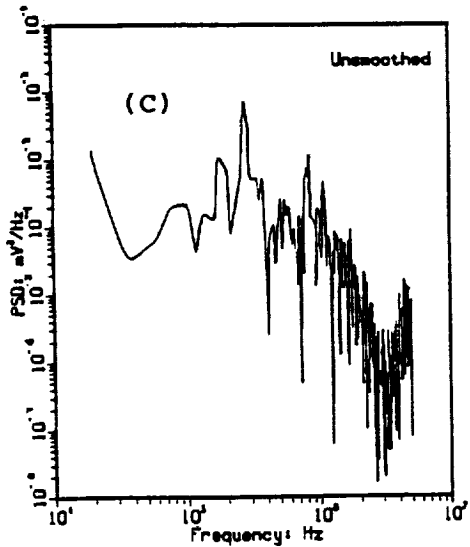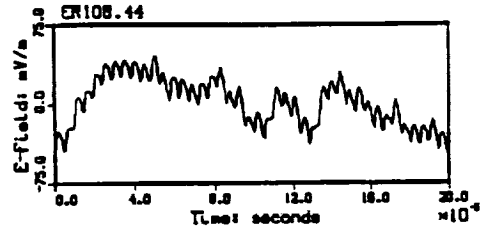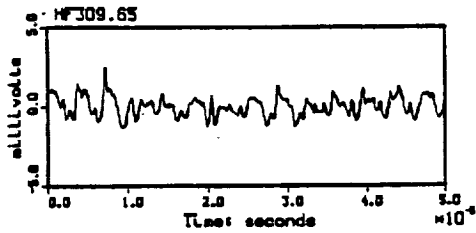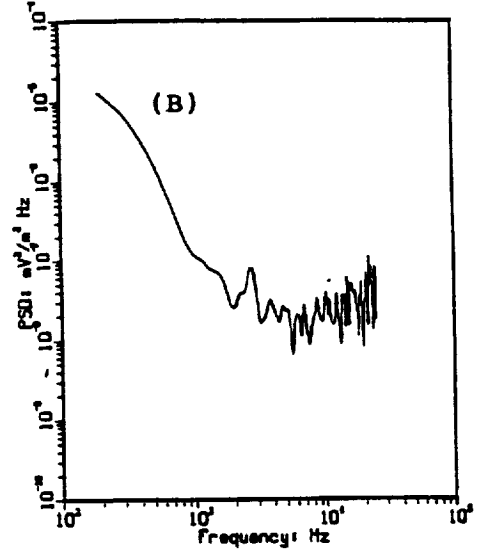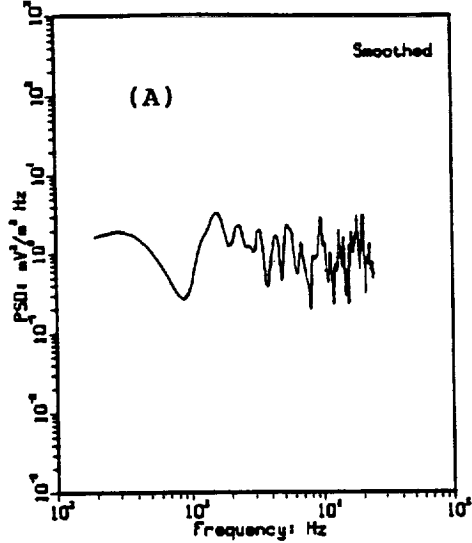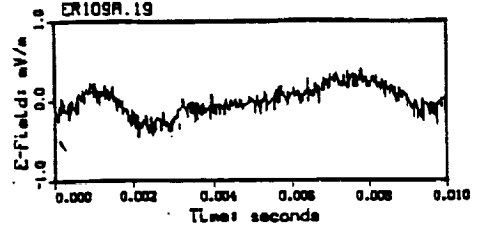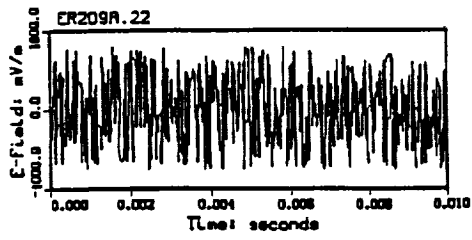
Figure 15. Selected observations of fluctuating electric fields (small upper panel) and associated spectral distributions (larger lower panel) under four different conditions in the laboratory hollow-cathode plasma investigation of Szuszczewicz et al.[60]

ultimately involve current flow across a sheath. This is indeed the case in the illustration of Fig. 14A, and certainly the case in a tethered system in which one end may have current flow dominated (or controlled) by a hollow-cathode-like device, while the other end relies primarily on sheath currents. In general, sheath currents can be small, limited in first order by the thermal currents in the ambient plasma and the size of the sheath. Currents across sheaths however, can be difficult to diagnose, and may in fact be dominated by a complicated set of non-linear effects. This possibility is highest for large potentials and large sheaths, giving rise to the need for a fairly complete understanding of active phenomena within the sheath and an accurate measurement of currents transferred from the plasma and collected at the spacecraft surface.

That a space vehicle can charge is an accepted fact, but accumulated experimental results on charging levels are mixed. In all cases however, the database suggests that the incorporation of mitigation techniques in spacecraft design is a prudent approach to safety and mission success. This is particularly true in high altitude and geosynchronous orbit, and with all particle-beam experiments regardless of ephemerides.

The fundamental issue in spaceborne applications of energetic-particle beams involves current conservation of the charged-particle component of the beam, *i.e.* the space vehicle can eject an energetic particle beam of I_B amperes only if the ambient plasma can provide an equal quantity of return current. (The closure path is analogous to that shown in Figure 14A, with current from the hollow-cathode replaced by currents emitted by an energetic charged-particle beam.) If there is no return current, a simple linear analysis suggests that a meter-size spherical body emitting a net 10 mA electron beam would be expected to charge to 9 kV in 0.1 ms. In order to avoid charging to high positive potentials (for a net electron current emission) relative to the ambient plasma, the vehicle must attract an equal quantity of return electron current from sources that include ambient plasma electrons, beam-produced secondaries, and possibly suprathermal electrons created by non-linear interactions. If the spacecraft charges to levels greater than local ionization potentials, additional ion-electron pairs can be created in the vehicle sheath.

An estimate of the return current available to a body of collecting surface S [m^2] from an ambient thermal plasma of density N_e and temperature T_e is given by:

$$I_\infty[ma] = \left(\frac{n_\infty[cm^{-3}]}{10^5}\right) \left(\frac{T_e[°K]}{1600}\right)^{1/2} S[m^2] \tag{24}$$

For collecting areas of order 1 m^2 and ambient plasma densities less than 10^6 cm^{-3}, this return current is less than 10 mA.[61] With ionospheric densities potentially as low as 10^3 cm^{-3}, this suggests that a prudent spacecraft design needs to emphasize the importance of total conducting surface area, even for very modest beam currents.

Charging to large vehicle potentials also raises concern with large plasma sheaths and attendant modification of the spacecraft's nearby plasma environment. Estimates for sheath sizes determined previously[62] were found to be adequately represented for

probe-like potentials by

$$(R_{sh} - R_{sc}) = \lambda_D \left[2.5 - 1.54 \exp\left(\frac{-0.32 R_{sc}}{\lambda_D} \right) \right] \left(\frac{e\Phi_{sc}}{kT_e} \right)^{1/2} \tag{25}$$

where R_{sh} and R_{sc} are the radii of the sheath and spacecraft, respectively, λ_D is the electron Debye length, and ϕ_{sc} is the spacecraft potential relative to the ambient plasma. For a spacecraft potential of only 130 volts, the sheath size can approach 7 meters in the low density limit of 10^3 cm^{-3}; and at 1300 volts (and 10^3 cm^{-3}) it approaches 21 meters. The corresponding sheath sizes at 10^6 are 21 cm and 70 cm, respectively.

An illustration of the large sheath scenario is presented in Fig. 16. The figure is intended to represent a cylindrical payload with its axis parallel to the ambient magnetic field. Assuming that one can define a discrete sheath edge at a radius R_{sh} and at a potential of $-V_{sh}$ with respect to the payload frame, electrons will be attracted from the ambient plasma and undergo an $E \times B$ driven orbit in passing from the plasma to the satellite surface. In striking the payload surface, there will be a broad range of incident angles, suggesting that skin-mounted detectors intended to determine sheath potential from an energy measurement of impinging particles, must be capable of full pitch angle resolution. It is clear that a detector with acceptance angles only aligned with the radius vector will give inaccurate measurements of sheath potentials and current collected by the spacecraft surface.

Time dependency in sheath size and potential growth is also an important factor. At moderate to low ionospheric densities (10^4 - 10^5 cm^{-3}) consider for example a cylindrical payload ($L = 30$ m, $d = 3$ m) oriented with respect to the magnetic field as illustrated in Fig. 16. If at a time defined as $t = 0$ an electron emitting beam is ejected parallel to $\vec{B}$, the payload would charge to levels in the 1 - 10 kV range within 150 μs. Results of numerical calculations for such a simulation, with a beam-on pulse of 150μs, are presented in Fig. 17 (adopted from Drobot et al.[63]. Other aspects of the simulation (not detailed here) also show that the entire system would be repleat with plasma oscillations, placing very severe constraints on "in situ" diagnostics within the sheath and on skin-mounted particle detectors attempting to resolve the energy of impinging particles and the total potential across the sheath. Such measurements are indeed a necessity if one is to achieve an understanding of the charging/discharging mechanism and beam-plasma current closure in the spacecraft-ionosphere system.

5. Comments and Conclusions

In addressing the realities of current collection in dynamic space plasma environments, we have treated theoretical and experimental issues. The overall conclusion points to the fact that there are a substantial number of challenges remaining for some of the more complex and dynamic systems, not the least of which involves energetic beam experiments and long tethered satellite systems. In many cases experimental techniques must be able to diagnose and account for simultaneous variations in electric fields, plasma densities, energy distribution functions and ion mass. Inevitably,
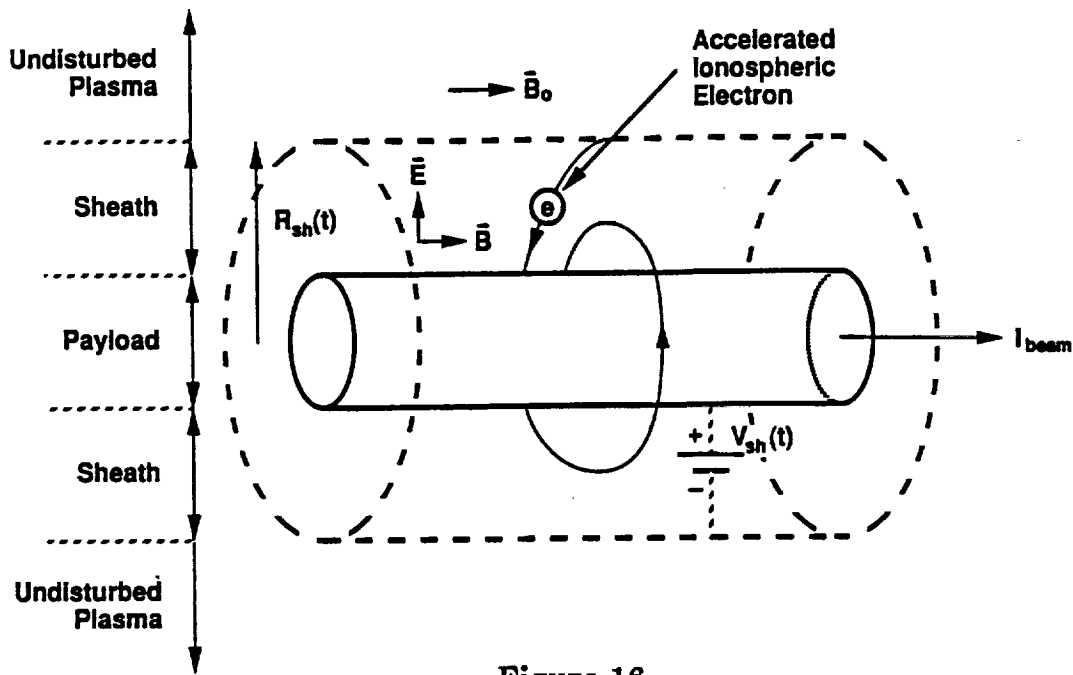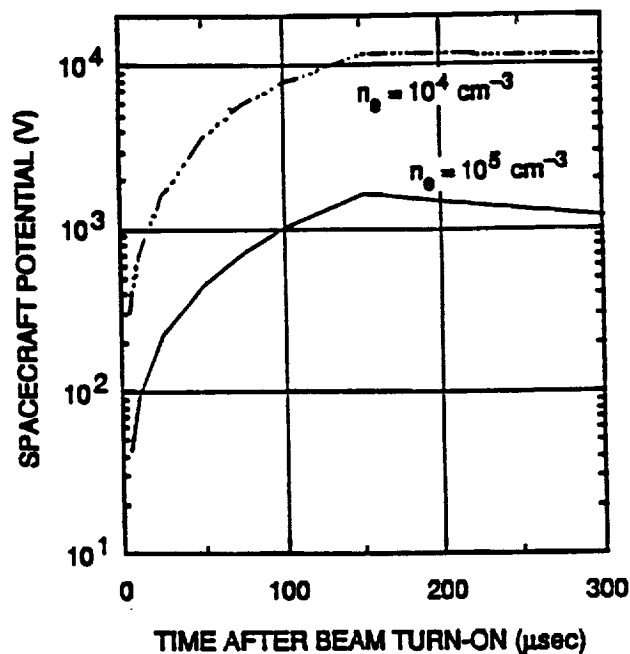
Figure 16

Figure 17. Time-dependent charging profile for a cylindrical payload (L,d) = (30m, 3m) oriented parallel to the geomagnetic field. The calculations assumed an energetic electron beam (I_B = 100 ma parallel to $\vec{B}$) with turn-on/turn-off at t=0/t=150 μs, respectively, and background ionospheric density states of 10^4 and 10^5 cm^{-3}. (Adapted from Drobot et al.[63])

most diagnostic systems assume that one or more of those variables is constant. In laboratory experiments there are times when this problem can be dealt with by virtue of experiment repeatability. This often is not the case in spaceborne experiments. At best there is some repeatability, but never comparable to that in a laboratory-based experiment. Ultimate success will rely on the development of new measurement techniques and a close synergism in theoretical developments and laboratory-based and spaceborne experiments.

References

1. Langmuir, I., and H. Mott-Smith, *Phys. Rev.* 28, 727 (1926).

2. Boyd, R.L.F., in *Plasma Diagnostics*, edited by W. Lochte-Holtgreven (North-Holland, Amsterdam, 1968), p. 732.

3. Chen, F.F., in *Plasma Diagnostic Techniques*, edited by R.H. Huddlestone and S.L. Leonard (Academic, New York, 1965), p. 113.

4. Szuszczewicz, E.P., "Area influences and floating potentials in Langmuir probe measurements," *J. Appl. Phys.* 43, 874 (1972).

5. Laframboise, J.G., University of Toronto Institute of Aerospace Studies Report No. 100 (1966) (unpublished).

6. Wehner, G., and G. Medicus, *J. Appl. Phys.* 23, 1035 (1952).

7. Hiroa, K., and K. Oyama, J. Geomagn, *Geoelectr.* 24, 415 (1972).

8. Szuszczewicz, E.P., and J.C. Holmes, "Surface contamination of active electrodes in plasmas: Distribution of conventional Langmuir probe measurements," *J. Appl. Phys.* 45, 5134 (1975).

9. Investigators who drive their proves with a ramp voltage function may never be aware that their measurements are distorted by surface effects.

10. See, for example, G.L. Gains, in *Scientific Foundations of Vacuum Techniques*, 2nd ed., edited by S. Dushman and J.M. Lafferty (Wiley, New York, 1966), p. 376; E.W. McDaniel, *Collision Phenomena in Ionized Gases*, (Wiley, New York, 1964), Chap. 13.

11. See, for example, H.F. Winters and P. Sigmund, *J. Appl. Phys.* 45, 4760 (1974).

12. J.C. Holmes and E.P. Szuszczewicz, *Rev. Sci. Instrum.* 46, 592 (1975).

13. Szuszczewicz, E.P., and J.C. Holmes, "Re-entry plasma diagnostics with a pulsed plasma probe," AIAA Paper No. 76-393, *AIAA 9th Fluid and Plasma Dynamics Confernece*, July 1976.

14. Szuszczewicz, E.P., "Laboratory simulation of controlled energetic electron-beam-plasma interactions in space," *AIAA J.* 21, 1374 (1983).

15. Szuszczewicz, E.P., "Controlled electron beam experiments in space and supporting laboratory experiments," *J. Atm. Terr. Phys.* 47, 1189 (1985).

16. Grossmann, W., D. Rault, A. Drobot, J. Bukson, J. Mimis and D. Buden, "Non-

nuclear megawatt pulsed power," *SAIC Rpt. to AFWAL*, February 1988.

17. Sanmartin, J.R., *Phys. Fluids* <u>13</u>, 103 (1970).

18. Brown, I.G., A.B. Compher, and W.B. Kunkel, *Phys. of Fluids* <u>14</u>, 1377 (1971).

19. Chen, F.F., C. Etievant and D. Mosher, *Phys. Fluids* <u>11</u>, 811 (1968).

20. Miller, N.J., *J. Geophys. Res.* <u>77</u>, 2851 (1972).

21. Laframboise, J.G., and J. Rubinstein, *Phys. Fluids* <u>19</u>, 1900 (1976).

22. Szuszczewicz, E.P. and P.Z. Takacs, *Phys. Fluids* <u>22</u>, 2424 (1979).

23. Waywouth, F., *J. Appl. Phys.* <u>37</u>, 4492 (1966).

24. Szuszczewicz, E.P., J.C. Holmes and M. Singh, *Astrophys. and Sp. Science* <u>86</u>, 235 (1982).

25. Hoegy, W.R. and L.J. Wharton, *J. Appl. Phys.* <u>44</u>, 5365 (1973).

26. McClure, J.P. and W.B. Hanson, *J. Geophys. Res.* <u>78</u>, 7431 (1973).

27. Keskinen, M.L., E.P. Szuszczewicz, S.L. Ossakow and J.C. Holmes, *J. Geophys. Res.* <u>84</u>, 17 (1979).

28. Baracat, W.A. and C.L. Butner, Tethers in Space Handbook, Bantam Books (1986).

29. Penzo, P.A., "A survey of tether applications to planetary exploration," NASA/ AIAA/PSN, Intl. Conf. on Tethers in Space, (17-19 September 1986).

30. Szuszczewicz, E.P., "Technical issues in the conduct of large space platform experiments in plasma physics and geoplasma sciences," invited paper presented at the NASA/JPL Workshop on "Space Technology Plasma Issues in 2001", September 24-26, 1986 (in the Proceedings, Jet Propulsion Laboratory, Pasadena, California; J. Feynman, H. Garrett, and S. Gabriel, editors, 1986)

31. Krishnan, M., R.G. Jahn, W.F. Von Jashowsky and K.E. Clark, "Physical processes in hollow cathodes," *AIAA J.* <u>15</u>, 1217 (1977).

32. Lidsky, L.M., S.D. Rothleder, D.J. Rose, S. Yoshikawa, C. Mishelson, and R.J. Machin, Jr., "Highly ionized hollow-cathode discharge," *J. Appl. Phys.* <u>33</u>, 2490 (1962).

33. Hastings, D.E., "The use of plasma contactors in the ionosphere," *J. Spacecraft and Rockets* (1986).

34. Duncan, B., A. Konradi, J. Raitt, J. R. Winkler, I. Katz, W. Nobles, N. Stone and E. C. Whipple, "Final report of the 'ad hoc' orbiter charging committee for the TSS-1 mission," USRA Publication (Nov. 25, 1985).

35. Hastings, D. E. and M. Martinez-Sanchez, "The use of electrodynamic tethers for generating power and thrust," *Proceedings of the 33rd Annual Meeting of the Am. Astronautical Society*, Boulder, CO (1986).

36. Davis, V.A., I. Katz, M.J. Mandell, and D.E. Parks, "Three-dimensional simulation of the operation of a hollow-cathode electron emitter on the shuttle orbiter,"

NASA/AIAA/PSN, *Intl. Conf. on Tethers in Space* (17-19 September 1986).

37. a) McCoy, J., "Electrodynamic interactions," in <u>Applications of Tethers in Space</u>, *NASA Conf. Publ. 2422*, NASA Scientific and Technical Information Branch (1986).

    b) McCoy, J., "Plasma motor/generator reference for power and propulsion," NASA/AIAA/PSN *Intl. Conf. on Tethers in Space*, Arlington, VA (September 18, 1986).

38. Wilbur, P., "Plasma contactor performance characterization," *NASA Conf. Publ. 2422*, NASA Scientific and Technical Information Branch (1986).

39. Gioulekas, A. and D. E. Hastings, "The role of current driven instabilities in the operation of plasma contactors used with electrodynamic tethers," *J. Propulsion and Power* (1989, in press).

40. Davidson, R.C., N.A. Krall, and R. Shanny, "Electron heating by electron-ion beam instabilities," *Phys. Rev. Lett.* <u>24</u>, 579 (1970).

41. Papadopoulos, K., "A review of anomalous resistivity for the ionosphere," *Rev. Geophys. and Space Phys.* <u>15</u>, 113 (1977).

42. Ishihara, O. and A. Hirose, "Non-linear evolution of Buneman instability," *Phys. Fluids* <u>24</u>, 452 (1981).

43. Davis, V. A., I. Katz, M. J. Mandell and D. E. Parks, "A model of electron collecting plasma contactors," in <u>Tethers in Space Toward Flight</u>, an AIAA Proceedings Publication on the Third Int'l Conf. on Tethers in Space (San Francisco, CA, May 1989), pp. 94-99, Paper # 89-1560-CP.

44. Iess, L., and M. Dobrowolny, "A fluid model of plasma contactors in the ionosphere," in <u>Tethers in Space Toward Flight</u>, an AIAA Proceedings Publication on the Third Int'l Conf. on Tethers in Space (San Francisco, CA, May 1989), pp. 70-76, Paper # 89-1557-CP.

45. Williams, J. D. and P. J. Wilbur, "Ground-based tests of hollow-cathode plasma contactors," in <u>Tethers in Space Toward Flight</u>, an AIAA Proceedings Publication on the Third Int'l Conf. on Tethers in Space (San Francisco, CA, May 1989), pp. 77-87, Paper # 89-1558-CP.

46. Vannaroni, G., C. B. Cosmovici, J. McCoy, C. Bonifazi, M. Dobrowolny, U. Guidoni, L. Iess, L. Scandurra, "Experimental characterization of hollow-cathode plasma sources at Fracatti," in <u>Space Tethers for Science in the Space Station Era</u>, ed. L. Guerriero and I. Bekey, Societa Italiana di Fisica, <u>14</u>, Bologna, Italy (Conf. Proceedings, Oct. 1987), pp. 254-260, published in 1988.

47. Patterson, M. J. and R. S. Aadland, "Ground-based plasma contactor characterization," in <u>Space Tethers for Science in the Space Station Era</u>, ed. L. Guerriero and I. Bekey, Societa Italiana di Fisica, <u>14</u>, Bologna, Italy (Conf. Proceedings, Oct. 1987), pp. 261-268, published in 1988.

48. Williams, J. D., P. J. Wilbur and J. M. Manheiser, "Experimental validation of a

phenomenological model of the plasma contacting process," in <u>Space Tethers for Science in the Space Station Era</u>, ed. L. Guerriero and I. Bekey, Societa Italiana di Fisica, <u>14</u>, Bologna, Italy (Conf. Proceedings, Oct. 1987), pp. 245-253.

49. Stenzel, R. L., R. Williams, R. Aguero, K. Kitazaki, A. Ling, T. McDonald, and J. Spitzer, *Rev. Sci. Instrum.* <u>53</u>, 1027 (1982).

50. Stenzel, R. L., W. Gekelman, and N. Wild, *Phys. Fluids* <u>26</u>, 1949 (1983).

51. Stenzel, R. L., W. Gekelman, and N. Wild, *J. Geophys. Res.* <u>88</u>, 4793 (1983).

52. Urretia, J. M. and R. L. Stenzel, "Waves and wings from tethers and electrodes in a laboratory plasma," in <u>Tethers in Space</u>, Conference Proceedings (AIAA/NASA/ASI/ESA, 17-19 May 1989), AIAA Publication (1989), p. 63.

53. Bernstein, W., H. Leinbach, H. Cohen, P. S. Wilson, T. N. Davis, T. Hallinan, B. Baker, J. Martz, R. Zeimke, W. Huber, "Laboratory observations of RF emissions at ω_{pe} and $(N + 1/2)\omega_{pe}$ in electron beam-plasma interactions," J. Geophys. Res. <u>80</u>, 4375 (1975).

54. Bernstein, W., H. Leinbach, P. Kellogg, S. Monson, T. Hallinan, O. K. Garriott, A. Konradi, J. McCoy, P. Daly, B. Baker and H. R. Anderson, "Electron beam experiments: the beam plasma discharge at low pressures and magnetic field strengths," *Geophys. Res. Lett.* <u>5</u>, 127 (1978).

55. Bernstein, W., H. Leinbach, P. J. Kellogg, S. J. Monson and T. Hallinan., "Further laboratory measurements of the beam-plasma-discharge," *J. Geophys. Res.* <u>84</u>, 7271 (1979).

56. Szuszczewicz, E. P., K. Papadopoulos, W. Bernstein, C. S. Lin and D. N. Walker, "Threshold criteria for a space-simulation beam-plasma-discharge," *J. Geophys. Res.* <u>87</u>, 1565 (1982).

57. Szuszczewicz, E. P., D. N. Walker, H. Leinbach, "Plasma diffusion in a space simulation beam-plasma-discharge," *Geophys. Res. Lett.* <u>6</u>, 201 (1979).

58. Kellogg, P. J., H. R. Anderson, W. Bernstein, T. J. Hallinan, R. H. Holzworth, R. J. Jost, H. Leinbach and E. P. Szuszczewicz, "Laboratory simulation of injection of particle beams in the ionosphere," in <u>Artificial Particle Beams in Space Plasma Studies</u>, B. Grandal, ed., Plenum Publishing Co., New York, pp. 289-329 (1982).

59. Kellogg, P. J. and R. W. Boswell, "Beam-plasma instabilities and the beam-plasma discharge," *Phys. Fluids* <u>29</u>, 1669 (1986).

60. Szuszczewicz, E. P., G. Earle, T. Bateman and J. McCoy, "Laboratory studies of electrostatic noise in a hollow-cathode plasma," *Geophys. Res. Lett.* (1989, in preparation).

61. Linson, L.M. and K. Papadopoulos, "Theoretical Support of the Spacelab Instrument/Experiment Definition of a Theoretical and Experimental Study of Beam-Plasma Physics (TEBPP)," Report No. LAPS 76/SAI-023-081-316-LJ, Science Applications Inc., La Jolla, California (Sept. 1981).

62. Szuszczewicz, E.P. and P.Z. Takacs, "Magnetosheath Effects on Cylindrical Lang-

muir Probes," *Phys. of Fluids* 22, 2424 (1979).

63. Drobot, A., K. Ko, L. Linson, R. Smith and E. P. Szuszczewicz, "Spacecraft Charging," in <u>The Neutral Particle Beam Program: Environmental Effects Analyses Threat Assessment Instrument Design, and Operational Considerations,</u> E. P. Szuszczewicz (ed.) SAIC/MCL-157-361-20-A, 19, 35 (1987).